

1 **Future permafrost degradation under climate change in a headwater catchment of Central**
2 **Siberia: quantitative assessment with a mechanistic modelling approach**

3 Thibault Xavier¹, Laurent Orgogozo^{1*}, Anatoly S. Prokushkin², Esteban Alonso-González³, Simon
4 Gascoin⁴, Oleg S. Pokrovsky^{1,5}

5 ¹Geoscience Environnement Toulouse (GET), CNRS, UMR5563, Toulouse, 31400, France

6 ²V.N. Sukachev Institute of Forest SB RAS, Russia

7 ³Instituto Pirenaico de Ecología, Consejo Superior de Investigaciones Científicas (IPE-CSIC), Jaca,
8 Spain

9 ⁴Centre d'Etudes Spatiales de la Biosphère, Université de Toulouse, CNRS/CNES/IRD/INRA/UPS,
10 Toulouse, France

11 ⁵BIO-GEO-CLIM Laboratory, Tomsk State University, Tomsk, Russia

12 * *Corresponding author*: Laurent Orgogozo (laurent.orgogozo@get.omp.eu)

13 **Abstract**

14 Permafrost thawing as a result of climate change has major consequences locally and globally for
15 the biosphere as well as for human activities. The quantification of its extent and dynamics under
16 different climate scenarios is needed to design local adaptation and mitigation measures and to
17 better understand permafrost climate feedbacks. To this end, numerical simulation can be used to
18 explore the response of soil **thermal and hydrological** regimes to changes in climatic conditions.
19 Mechanistic approaches minimize modelling assumptions by relying on the numerical resolution
20 of continuum mechanics equations, but they involve significant computational effort. In this work,
21 the permaFoam solver is used along with high-performance computing resources to assess the
22 impact of four climate scenarios of the Coupled Model Intercomparison Project –Phase 6 (CMIP6)
23 on permafrost dynamics within a pristine, forest-dominated watershed in the continuous permafrost
24 zone. Using these century time-scale simulations, changes in the soil temperature, soil moisture,
25 active layer thickness and water fluxes are quantified, assuming no change in the vegetation cover.
26 The most severe scenario (SSP5-8.5) suggests a dramatic increase in both the active layer thickness
27 and annual evapotranspiration, with the maximum values on the watershed ~~reached~~ in 2100 ~~of~~
28 **increasing by +65% and +35%—increases compared to current conditions**, respectively. For the
29 active layer thickness, **a variable that integrates both the thermal and hydrological states of the near-**
30 **surface permafrost, this projected increase would correspond to a ~350 km southward shift in**
31 **current climatic conditions**. Moreover, in this scenario, the thermal equilibrium of near-surface
32 permafrost with the new climatic conditions would not be reached in 2100, suggesting a further
33 thawing of permafrost even in the case of halt of in which the climate change is halted.

34 **Keywords**

35 Permafrost, climate change, boreal forest, numerical modelling, high performance computing, soil
36 temperature, soil moisture, evapotranspiration.

37

38 **1 Introduction**

39

40 Permafrost is mostly situated in regions that are experiencing especially intense climate
41 change, resulting in widespread warming and thawing, with the shrinking of its lateral extension
42 and the thickening of the soil active layer (Biskaborn et al., 2019; Hu et al., 2022; Li et al., 2022a,
43 2022b). Permafrost thawing induces sizable changes in the environments (Walvoord and Kurylyk,
44 2016; Nitze et al., 2018; Makarieva et al., 2019; Jin et al., 2022; Wright et al., 2022) and for
45 human activities (Shiklomanov et al., 2017; Strelestkiy et al., 2019, 2023; Hjort et al., 2018, 2022)
46 in the Arctic and the sub-Arctic. For instance, a permafrost-thaw-related decrease of in the soil
47 moisture leads to an increase in boreal fire frequency (Kurylyk, 2019; Kim et al., 2020), while soil
48 mechanical instabilities induced by permafrost thawing threaten population-human settlements
49 (Ramage et al., 2021) and infrastructures (Bartsch et al., 2021). Moreover, permafrost thaw may
50 exert significant controls on the biogeochemical cycles of carbon and related metals (Sonke et al.,
51 2018; Karlsson et al., 2021; Walvoord and Striegl, 2021) and climate dynamics (Miner et al.,
52 2022; Park and Kug, 2022; de Vrese et al., 2023), with potentially major feedback on climate
53 warming. Thus, anticipating the evolution of permafrost cover and dynamics is of primary
54 importance for understanding and mitigating the climate-change-induced impacts at high latitudes.
55 For this, robust and accurate numerical simulations are required (Schneider von Deimling et al.,
56 2022; Hu et al., 2023b).

57 Boreal forest is one of the largest biomes on Earth (Gauthier et al., 2015), and 80% of its
58 area is located in permafrost regions, where it covers 55% of the territory (Stuenzi et al., 2021).
59 Due to the complexity of the biophysical processes involved, quantifying the evolution of
60 permafrost dynamics in boreal forests under climate change requires mechanistic, high-resolution
61 modelling approaches (Orgogozo et al., 2019). However, the large extent of the considered areas
62 makes the use of such approaches impracticable at global, continental or regional scales. As a
63 consequence, the mechanistic modelling of permafrost dynamics has to focus on processes at the
64 watershed scale in headwater catchments with long-term environmental monitoring, following a

65 | general trend in the Arctic sciences (Speetjens et al., 2023; Vonk et al., 2023). In Arctic
66 | environments, the vegetation strongly controls the surface energy budget (Fedorov et al., 2019;
67 | Oehri et al., 2022), interacts with climate dynamics (Park et al., 2020; Kirilyanov et al., 2024) and
68 | drives water fluxes (Orgogozo et al., 2019). As such, vegetation should be taken into account when
69 | simulating the impact of climate warming on permafrost in boreal forest areas (Lorantý et al., 2018,
70 | Kirilyanov et al., 2020; Holloway et al., 2020).

71 | The quantitative mechanistic modeling of permafrost dynamics under climate change at the
72 | headwater catchment scale requires large computational resources, because fine spatio-temporal
73 | discretization is needed due to the strong non-linearities and couplings of various physical processes
74 | (Kurylyk and Watanabe, 2013). This is especially important for century long simulation periods
75 | (O'Neill et al., 2016) and simulation domains with surfaces of up to tens of square kilometres
76 | (e.g.: Arndal and Torp-Jørgensen, 2020). For this, high performance computing techniques are
77 | needed (Orgogozo et al., 2023).

78 | In this study, we focus on a permafrost-dominated, forested watershed of central Siberia
79 | which ~~that~~ was subjected to long-term environmental monitoring, the Kulingdakan watershed (e.g.:
80 | Prokushkin et al., 2007; Mashukov et al., 2021). The objective is to assess the future state of the
81 | permafrost and the ground thermal regime in this continuous-permafrost, boreal forest environment
82 | under different climate change scenarios at the century time scale. The permafrost status of this
83 | catchment under current climatic conditions has already been investigated (Orgogozo et al., 2019).
84 | Here, we simulate, using a mechanistic modelling approach, the permafrost dynamics at the
85 | catchment scale until 2100 under various scenarios of climate change. The vegetation controls on
86 | permafrost dynamics are partly included in the mechanistic modelling framework, considering
87 | evapotranspiration fluxes (Orgogozo et al., 2019), and partly handled empirically, via accounting
88 | ~~on~~ for the insulating effect of ground-floor vegetation (Blok et al., 2011; Cazaurang et al., 2023).
89 | However, because no changes ~~of~~ in vegetation ~~is~~ are explicitly considered, we assume constant
90 | biomass and primary production and therefore investigate only the physical part of the response of
91 | permafrost to climate change. We use the permaFoam High Performance Computing
92 | cryohydrogeological simulator (Orgogozo et al., 2023) with a national-level supercomputing
93 | infrastructure, the Joliot-Curie supercomputer of the Très Grand Centre de Calcul (TGCC) of the
94 | French Alternative Energies and Atomic Energy Commission (CEA). The simulated permafrost
95 | thawing features in Kulingdakan are discussed and compared for ~~the~~ different CMIP6 scenarios,
96 | including the following:

97 | - the soil thermal regime (soil temperature and active layer thickness evolution, equivalent
98 | southward shift under current climatic conditions);
99 | - the soil hydrology (evapotranspiration fluxes and soil moisture evolution);
100 | - the spatial variability of climate warming impacts at the scale of the watershed under study;
101 | - ~~and finally,~~ the state and evolution of the thermal imbalance of the permafrost- (e.g.: Ji et al.,
102 | 2022.; Nitzbon et al., 2023) in the considered region.

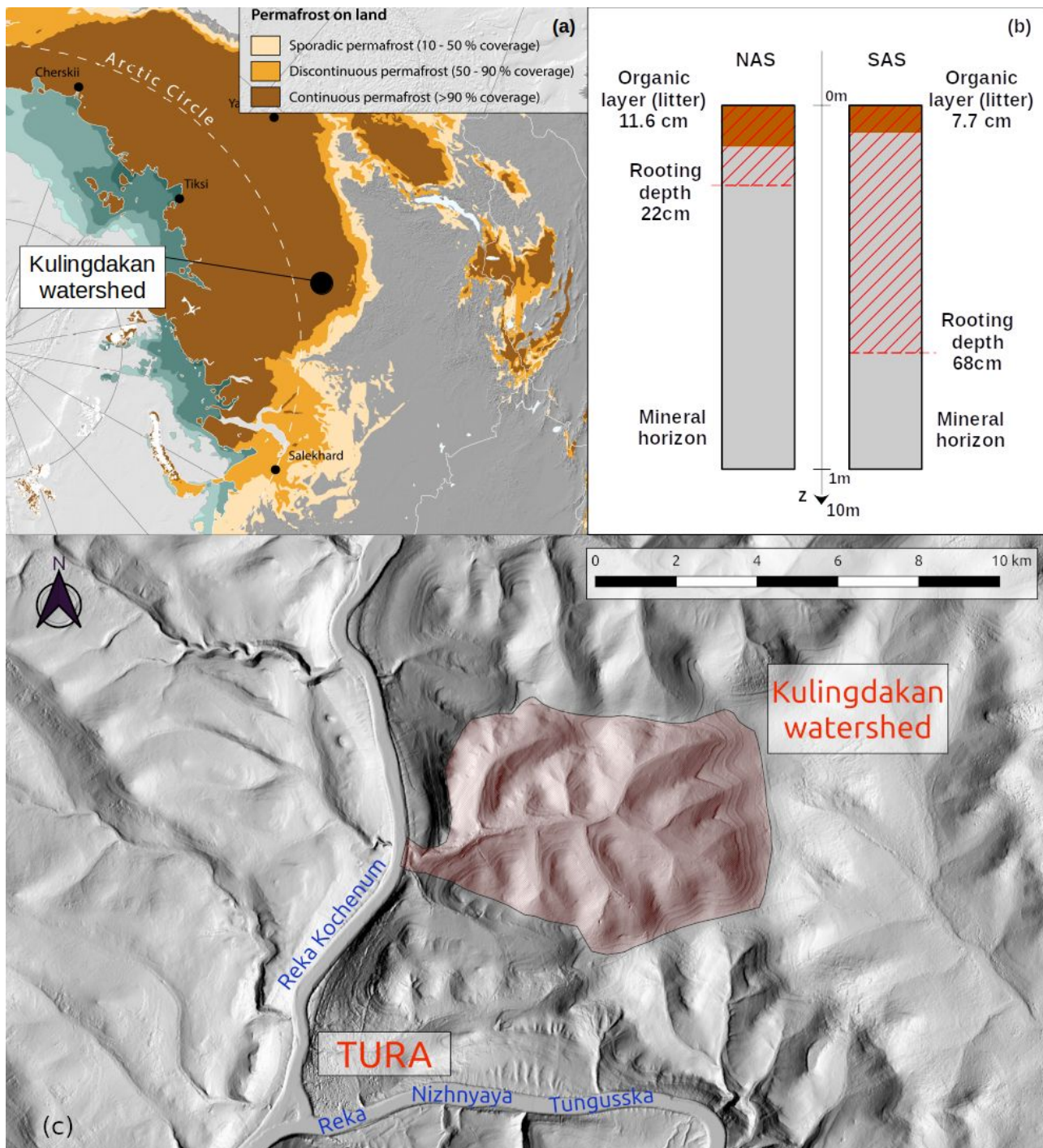
103 | 2 Materials and methods

104 | 2.1 Study site: Kulingdakan, a forested catchment in continuous-~~permafrost~~ area

105 | The Kulingdakan catchment is located in the Krasnoïarsk Rregion (64.31°N, 100.28°E),
106 | within a continuous permafrost zone, belonging to the boreal forest biome (Northern Taïga – see
107 | Figure, 1a). This pristine catchment is-has been monitored for the study of boreal processes over the
108 | past two decades. The vegetation is dominated by larch (*Larix gmelinii*), dwarf shrubs, mosses and
109 | lichens. The catchment covers an area of 41 km² and has an elevation ranging from 132 m to 630 m
110 | (Prokushkin et al., 2004). The climate is cold and continental, with an average annual mean
111 | temperature of -8°C and an annual total precipitation of 400 mm (annual mean measured between
112 | 1999 and 2014 at the Tura meteorological station, 5 km south of the Kulingdakan catchment,
113 | altitude of 168 m-~~altitude~~). The stream, which flows from east to west, divides the 41 km²
114 | catchment area into two approximately rectangular slopes of equal area, the North Aspect Slope
115 | (NAS) and the South Aspect Slope (SAS). As shown by a previous numerical study withusing
116 | permaFoam of this site under current climatic conditions, the hydrological budget in this watershed
117 | is largely dominated by evapotranspiration fluxes (Orgogozo et al., 2019). Two horizons constitute
118 | the soil in the first few meteres: an organic horizon (litter and peat) and a mineral horizon (mainly
119 | rocky/gravelly loam).

120 | Due to the difference in solar radiation induced by their aspects, primary production and
121 | evapotranspiration are more intensive in the SAS than in the NAS. Thus the two slopes show
122 | significant differences; in the larch trees size and larch stands density, as well as in the rooting
123 | depth, organic horizon and moss layer thickness and active layer dynamics. The thickness of the
124 | organic horizon is ~~of~~ 11.6 cm on the NAS and 7.7 cm on the SAS (Gentsch, 2011), while the moss
125 | layer thickness is ~~of~~ 13 cm on the NAS and 6.4 cm on the SAS (Prokushkin et al., 2007). The
126 | rooting depth is ~~of~~ 10 cm into the mineral horizon for the NAS; and 60 cm for the SAS (Viers et al.,
127 | 2013), and this difference has been shown to be of great importance for the dynamics of the active

128 layer (Orgogozo et al., 2019). The observed maximum active layer thickness is of 1.22 m in the
 129 SAS and of 0.58 m in the NAS (Gentsch, 2011). These pedological and physiological contrasts
 130 between the two aspects of the watershed slope, summarized in Figure 1b, are explicitly considered
 131 when performing permafrost simulations (Supplementary Material B).
 132



133 **Figure 1: (a) Location of Kulingdakan watershed (map from GRID-Arendal/Nunataryuk). (b)**
 134 **Representation of soil column structure for North Aspected Slope (NAS) and South**

135 | **Aspected sSlope (SAS) of the Kulingdakan watershed. (c) Digital Elevation Model (DEM) of**
136 | **Kulingdakan watershed, extracted from ArcticDEM (Porter et al., 2023).**

137 | Previous modelling studies in the Kulingdakan catchment on water fluxes repartition, the
138 | soil temperature at different depths and the active layer thickness (Orgogozo et al., 2019; Orgogozo
139 | et al., 2023) demonstrated that the use of the permaFoam solver, together with boundary conditions
140 | (water fluxes and soil surface temperature) provided by field measurements, enabledmade it
141 | possible to obtain numerical simulation results in agreement with in-situ observations under current
142 | climatic conditions .

143 | 2.2 The permaFoam cryohydrogeological simulator

144 | The numerical tool used in this study is permaFoam (Orgogozo et al., 2019, 2023), the
145 | permafrost modelling solver developed in the framework of OpenFOAM, the open source, high
146 | performance computing tool box for computational fluid dynamics (Weller et al., 1998,
147 | openfoam.org, openfoam.com). This solver is designed to simulate 3D, transient coupled heat and
148 | water transfers in a variably saturated soil with evapotranspiration and the freezeing/thawing of the
149 | pore water. The two main equations solved by permaFoam are the Richards equation (Eq. (1)),
150 | which-that governs the flow of water, and an energy balance equation (Eq. (2)) that governs the heat
151 | transfer; both are defined at the Darcy scale of the considered porous medium (soil):

152

$$C_H(h) \frac{\partial h}{\partial t} = \nabla \cdot (K_H(h, T) \cdot \nabla (h+z)) + Q_{AET}(h, t) \quad (1)$$

$$\frac{\partial \left(\left(C_{T,eq}(h, T) + L \frac{\partial \theta_{ice}(h, T)}{\partial T} \right) T \right)}{\partial t} + \nabla \cdot (V(h, T) C_{T,liquid} T) = \nabla \cdot (K_{T,eq}(h, T) \nabla T) \quad (2)$$

153

154 | The two primary variables in equationsEqs. (1) and (2) are the generalizesed water pressure head h
155 | [m] and the soil temperature T [K], respectively. In the Richards equation (Eq. (1)), z is the vertical
156 | coordinate [m] (oriented upward), K_H is the hydraulic conductivity of the variably saturated,
157 | variably frozen porous medium [$m \cdot s^{-1}$], C_H is the capillary capacity (also called the specific moisture
158 | capacity) of the unsaturated porous medium [m^{-1}] and Q_{AET} [s^{-1}] is a source term representing the
159 | water uptake by the vegetation through the evapotranspiration process (computed using the Hamon
160 | formula; see Hamon, 1963; Frolking, 1997). From the pressure head field h , the Darcy velocity V
161 | [$m \cdot s^{-1}$] is derived according to equationEq. (3):

$$V(h, T) = K_H(h, T) \cdot \nabla(h+z) \quad (3)$$

162

163 | In the energy balance equation (Eq. (2)), the considered transfer processes are conduction through
 164 | the entire porous medium, convection by pore water flow, and latent heat exchanges when phase
 165 | changes occurs. In this heat transfer equation, $K_{T,eq}$ [$J \cdot m^{-1} \cdot s^{-1} \cdot K^{-1}$] is the apparent thermal
 166 | conductivity of the porous medium, θ_{ice} [-] is the volumetric ice content, L [$J \cdot m^{-3}$] is the latent heat
 167 | of fusion of ice, $C_{T,eq}$ [$J \cdot m^{-3} \cdot K^{-1}$] is the equivalent heat capacity of the porous medium, and $C_{T,liquid}$
 168 | [$J \cdot m^{-3} \cdot K^{-1}$] is the equivalent heat capacity of liquid water. In permaFoam these two coupled equations
 169 | are solved in 3D using the finite volumes method, with sequential operator splitting for handling the
 170 | couplings, Picard loops for dealing with the non-linearities, and a backward time scheme for
 171 | temporal discretization. A detailed description of the solver and can be found in Orgogozo et al.
 172 | (2023).

173 | The numerical resolution of these coupled and highly non-linear equations, including stiff
 174 | fronts generated by freeze/thaw processes, at the space and time scales required for studying climate
 175 | change impacts on boreal watersheds, requires both a robust algorithm and the efficient use of high
 176 | performance computing means. This is the reason why that permaFoam is developed within the
 177 | OpenFOAM framework, which allows benefiting the use of from up-to-date and efficient numerical
 178 | methods for solving partial differential equations on last-generation supercomputing facilities.
 179 | Thanks to its implementation in OpenFOAM, the permaFoam solver has demonstrated excellent
 180 | parallel performances on various supercomputer architectures with for dedicated test cases
 181 | (Orgogozo et al., 2023), both in terms of large numerical domains (up to 1 billion mesh points on
 182 | the CALMIP Olympe supercomputer) and the number of cores (16,000 on the GENCI IRENE-
 183 | ROME supercomputer).

184

185 **2.3 Modelling domain**

186 | According to preliminary numerical experiments (data not shown), for modelling
 187 | Kulingdakan watershed permafrost the use of a dual 2D simplified representation (Orgogozo et al.,
 188 | 2019) allows makes it possible to simulate properly the thermal and hydrological fluxes in the soils.
 189 | As such, full 3D simulations, which are far more costly from a computational prospect perspective
 190 | than 2D simulations (Orgogozo et al., 2023), are not needed. Besides Additionally, the use of 2D
 191 | simulations allows the consideration of lateral transfers (Sjöberg et al., 2016; Lamontagne-

192 Hallé et al., 2018, Hamm and Frampton, 2021, Jan, 2022). Thus, in this work we used 2D
193 numerical domains, with climatic forcing ~~as as the~~ top boundary conditions (see section 2.4) and
194 geothermal heat flux and nil water flux as ~~the~~ bottom boundary conditions. The initial conditions
195 were obtained by 10 years of spin-up under current climatic conditions. These current climatic
196 conditions were represented by a synthetic year of climate forcing corresponding to the multi-
197 annual means of the 1999–2014 observations (see Supplementary ~~m~~Material A, including Fig. S1).
198 The starting conditions of this spin-up were ~~the~~ extracted from ~~the~~ results of the previous
199 calculations (Orgogozo et al., 2019). ~~The convergence criterion for the spin-up was the active layer~~
200 ~~thickness inter-annual difference (annual variability less than 0.2%). The spatial discretisation of~~
201 ~~the domain is done using a mesh of 5.2×10^7 cells, according to a convergence study presented in~~
202 ~~Supplementary ~~m~~Material B.~~

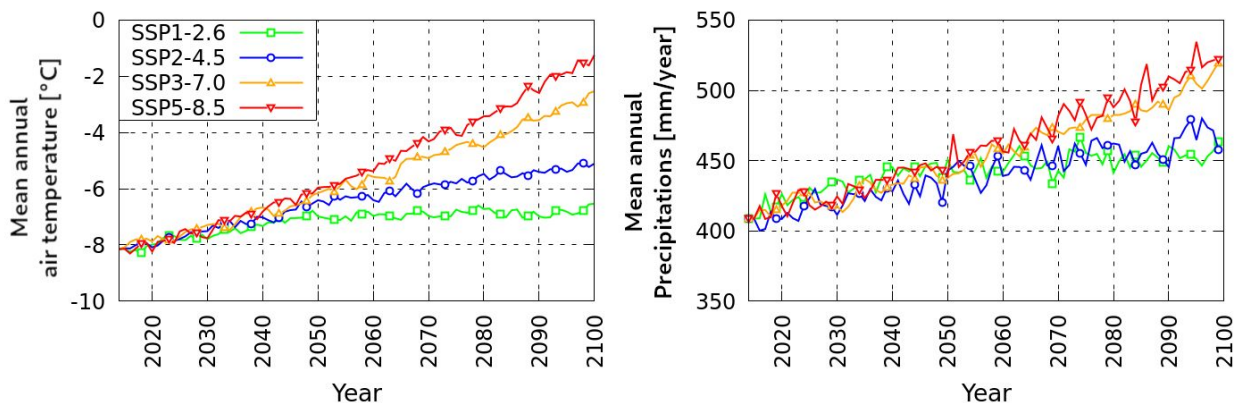
203 The numerical simulations provide the full 2D fields of physical quantities describing the
204 heat and water flow within ~~the~~ both ~~the~~ SAS and NAS (two 2.5-km-wide, 10-m-thick slopes),
205 including both ~~the~~ frozen and active layers in each slope. These included ~~the~~ soil temperature,
206 pressure head, liquid water content and ice content for each time step ~~that was of saving saved~~ (user
207 defined; here, ~~each~~every 6 months). In addition, ~~the~~ temperature, water content, ice content and
208 evapotranspiration sink term are monitored at ~~an~~ hourly frequency throughout two vertical profiles
209 located at ~~the~~ mid-slope of ~~the~~ SAS and NAS numerical domains, using 61 virtual point probes
210 distributed over the ~~ten-10 meters~~ of the numerical domain thickness. Finally, the infiltration and
211 exfiltration water fluxes through the total soil surface are also saved from the standard output at
212 every time step. Further details of modelling set up are presented in Supplementary material B.

213 **2.4 Soil surface conditions under climate change derived from CMIP6 scenarios**

214 In order to apply climate forcings that are representative of possible future trajectories, we
215 consider climate scenarios produced as a part of the Coupled Model Intercomparison Project Phase
216 6 (CMIP6) organized by the Intergovernmental Panel on Climate Change (IPCC) (Eyring et al.,
217 2016); ~~and~~ in particular, ~~we consider~~ the so-called tier-1, key scenarios (O'Neill et al., 2016). These
218 scenarios have been highlighted because of their relevance to scientific questions, the range of
219 possible futures they cover, and their continuity with previous ~~representative common pathways~~
220 (RCP) scenarios (~~Representative Concentration Pathways~~, van Vuuren et al., 2011) published
221 during CMIP5. We considered four CMIP6 scenarios, ~~from the most low-forcing sustainable~~
222 ~~pathway with the least forcing (coldest) to the most high-end forcing pathway with the most forcing~~

223 (hottest): SSP1-2.6, SSP2-4.5, SSP3-7.0 and SSP5-8.5. Among these scenarios, the SSP2-4.5 is the
 224 one most often used in permafrost studies (e.g.: Karjalainen et al., 2019; Ramage et al., 2021;
 225 Hjort et al., 2022). For each of these scenarios, an ensemble of models has been run on different
 226 regions of the globe. The climate model output data were accessed via the IPCC Working Group I
 227 (IPCC-WGI) Interactive Atlas (Iturbide et al., 2021), February 2023 version, which provides the
 228 median (P50) of the ensemble of models for a selected output variable, region and scenarios. We
 229 used the projections of the air temperature and precipitation changes for the East Siberian region,
 230 averaged at each yearly time step. For To obtaining the local scenarios of climate change for the air
 231 temperature and precipitation (Fig. 2), these yearly averaged projections of air temperature /
 232 precipitation changes between 2015 and 2100 have been summed with daily air temperature /
 233 precipitation variations along the synthetic year of climate forcing corresponding to the multi-
 234 annual means of the 1999–2014 observations in Tura, which are representative of current climatic
 235 conditions (see Supplementary Material A, Figure S1). This provided the projections of the daily
 236 air temperature / precipitation from 2015 to 2100 for the Tura area. The yearly averages of these
 237 daily projections are presented in Figure 2.

238



239

240 **Figure 2: Projections of air temperature and precipitation in Kulingdakan based on CMIP6**
 241 **projections on the Eastern Siberia area.**

242 The projections show an increase in the air temperature over the century, with a rate
 243 between $+1.9^{\circ}\text{C}/100$ years (SSP1-2.6) and $+7.8^{\circ}\text{C}/100$ years (SSP5-8.5); these rates were
 244 obtained by re-scaling the averaged increase rates from 2014 to 2100 to the centennial time scale.
 245 For every scenario this local increase rate is higher than the global one (global increase rates,
 246 according to Fan et al., [2020]: SSP1-2.6: $+1.18^{\circ}\text{C}/100$ years; SSP2-4.5: $+3.22^{\circ}\text{C}/100$ years;
 247 SSP3-7.0: $+5.50^{\circ}\text{C}/100$ years; SSP5-8.5: $+7.20^{\circ}\text{C}/100$ years). The Annual precipitation could

248 also change significantly, with a relative increase in 2100 of +12% (SSP1-2.6) to +29% (SSP5-8.5)
249 compared to the current value.

250 In order to translate these climate projections, ~~that~~which describe atmospheric conditions,
251 into suitable soil surface boundary conditions for cryohydrogeological simulations (water fluxes
252 and temperature at the soil surface, beneath snow and moss layers), a dedicated empirical procedure
253 has been developed. The goal is to set up a methodology for deriving the soil surface temperature
254 from the air temperature ~~ion~~ on the slopes of the Kulingdakan watershed, based on the available
255 observation data. Indeed, the soil temperature and air temperature may be significantly different in
256 such a boreal forest environment, due to the effects of understorey (Zellweger et al., 2019; Haesen
257 et al., 2021), moss cover insulation (Blok et al., 2011; Cazaurang et al., 2023), the winter snowpack
258 (Jan and Painter, 2020; Khani et al., 2023) and its interactions with vegetation (Dominé et al.,
259 2022). This empirical, site-specific procedure is detailed in Supplementary ~~m~~Material A, and it
260 ~~allows-makes it possible~~ to build up ~~a~~ slope-wise soil temperature estimates on the basis of the air
261 temperature and snow conditions. For water fluxes, the simplest approximation has been adopted,
262 assuming that the water flux at the top of the soil is equal to the rain flux. For the soil surface
263 temperature estimate, we first used a modified temperature index approach (Braithwaite and
264 Olesen; 1989, Hock 2003) for estimating the snow water equivalent, and then ~~awe used~~ multiple
265 regression ~~for~~to derivinge below ~~–~~moss; soil surface temperature from the air temperature,
266 precipitation and snow water equivalent. We chose a temperature index approach to simulate the
267 snow water equivalent on the soil surface because climate projections only provide the air
268 temperature and precipitation, whereas a more advanced energy balance snowpack model requires
269 additional information on wind, radiation, and air humidity. To calibrate this temperature index
270 model we first reconstructed ~~ed~~ the snow water equivalent for the period 1999–2014 from the
271 observed snow depth with the Multiple Snow Data Assimilation System (MuSA) toolbox (Alonso-
272 González et al., 2022) forced with ERA5 data (Hersbach et al., 2020), fusing available snow depth
273 observations with an ensemble of simulations generated by the energy and mass balance model
274 called the Flexible Snow Model (Essery, 2015). Then, we calibrated a multiple regression method
275 to derive the soil surface temperature as a function of the air temperature and precipitation, while
276 taking into account the insulating effect of moss and snow layers ~~insulating-effect~~. Calibrations
277 were performed with air temperature and precipitation data measurements, ~~and the~~ MuSA-
278 derived snow water equivalent between 1999 and 2014; and the top-~~soil~~ (i.e.; below moss) temperature
279 measured in situ between 2003 and 2005. With this procedure, for each slope, an empirical transfer

280 function that provides soil temperature estimates derived from the air temperature and precipitation
281 was obtained. Finally, these transfer functions were used to produce scenarios of the daily soil
282 surface temperature under climate change for the two slopes of the catchment. This information
283 ~~was~~ needed to for building the soil surface boundary conditions of the hydrogeological
284 simulations. It must be emphasized that our empirical approach was based on parametrical fitting
285 on observation data for estimating the transfer function between atmospheric forcing and the soil
286 surface temperature. As a result, no vegetation changes ~~along due to~~ climate change could be
287 considered in this transfer function. Therefore, we focused on the purely physical response of the
288 catchment permafrost to climate change, while considering the vegetation impacts on permafrost
289 dynamics at constant vegetation cover. Coupling a vegetation dynamics with the
290 cryohydrogeological model would allow one to assess the impact of the climate warming-induced
291 changes of the vegetation cover on permafrost conditions. However, this is beyond the scope of the
292 present study and will be the focus of future works.

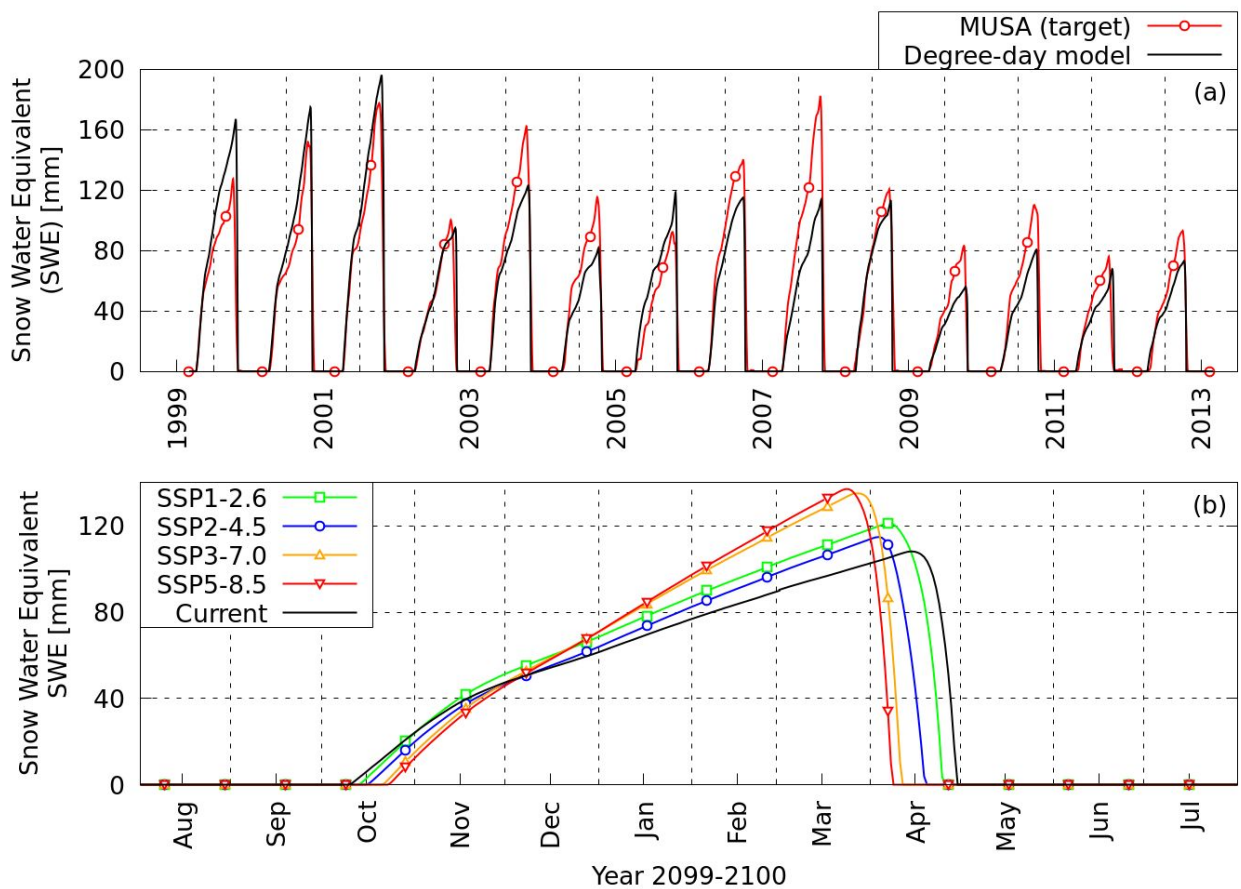
293 **3 Results**

294
295 From ~~P~~post-processing the computed 2D fields of physical quantities describing the heat and water
296 flow within ~~the~~ both the SAS and NAS (two 2.5-km-wide, 10-m-thick slopes), including both
297 frozen and active layers in each slope, a large wealth of data characterizing the considered virtual
298 permafrost dynamics is obtained (Supplementary ~~m~~Material C), and below, only the key features of
299 the centennial evolution under climate change are presented.

301 **3.1 Soil surface temperature projections**

302 The results of the temperature index approach used for modelling the snow cover of the
303 Kulingdakan watershed is presented in Figure 3. The snow water equivalent (SWE) model shows a
304 good agreement with the MuSA reconstructions (Figure, 3a); hence, this model was used to
305 estimate the SWE under future climate projections (Figure 3b).

306

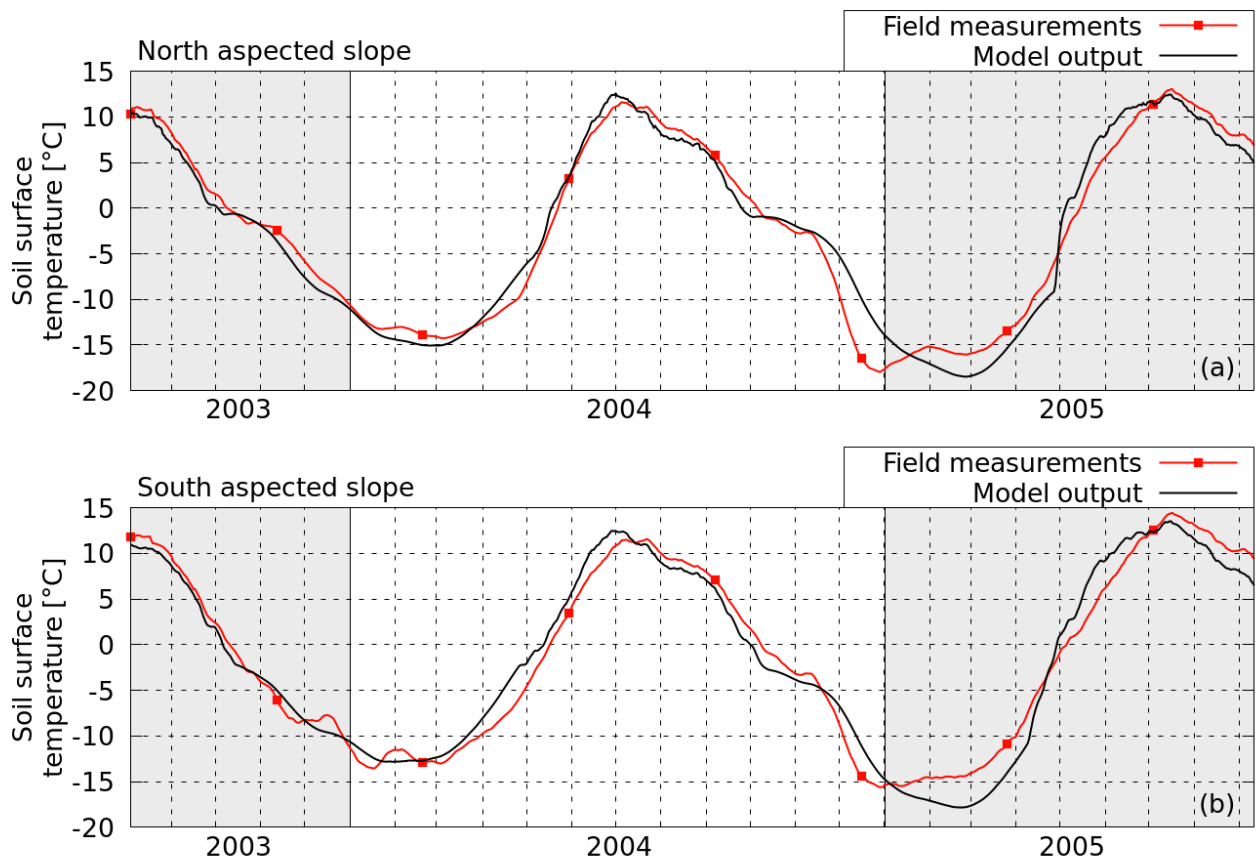


307

308 **Figure 3: (a) Present snow model comparison with MuSA output (a) and (b) projection at the**
 309 **end of the century (b).**

310 For each slope, the output data of the snow cover model were used as input data for the multiple
 311 regression of the soil surface temperature, alongside with the air temperature data and precipitation
 312 data. These empirical transfer functions were in good agreement with the observations, as shown
 313 in Figure 4.

314

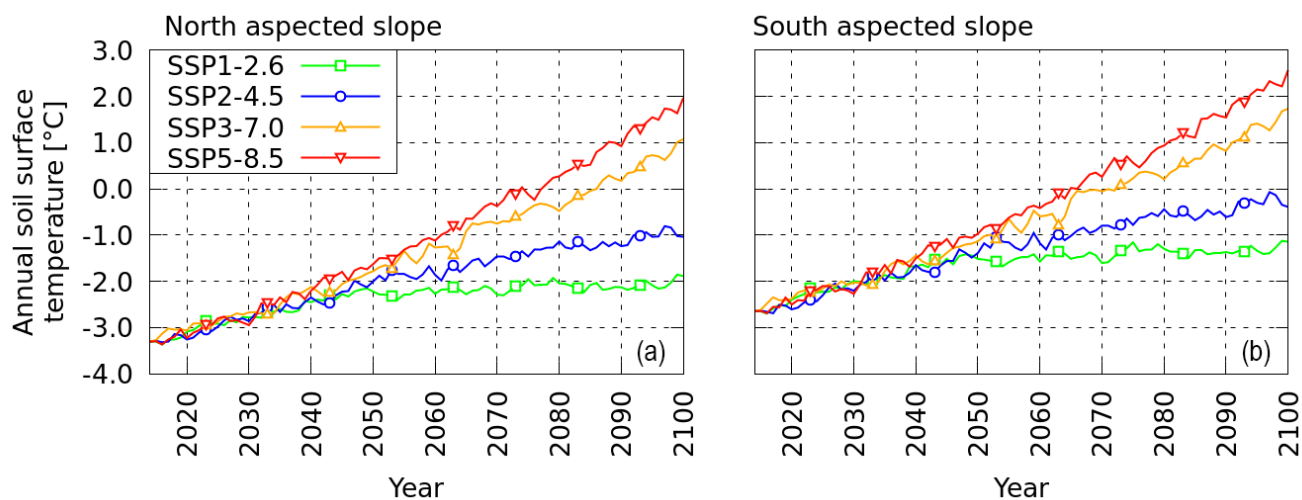


315

316 **Figure 4: Measurements and empirical transfer function estimates for soil surface**
 317 **temperature in present climatic conditions in (a) NAS (a) and (b) in SAS (b).**

318 The L1 norm of the differences between the field measurements and model output is $\approx 1.42^\circ\text{C}$ in
 319 the NAS, and $\approx 1.56^\circ\text{C}$ in the SAS. The L2 norms of these differences are $\approx 0.07^\circ\text{C}$ for both the
 320 SAS and NAS. A more detailed discussion of the behaviour of these empirical transfer functions
 321 may be found in Supplementary Material A.

322 Finally, for each slope, soil temperature projections are obtained for the four considered CMIP6
 323 climate scenarios by applying the developed modeling chain with the projections for air
 324 temperature and precipitation as input data.



325

326 **Figure 5: Soil surface temperature projections over the century based on SSP scenarios**
 327 **obtained using the transfer function described in Supplementary Material A. Transfer**
 328 **function model estimation for soil surface temperature at present conditions for (a) north-**
 329 **aspected-slope (a) the NAS and (b) SAS south-aspected-slope of the Kulingdakan watershed (b).**

330

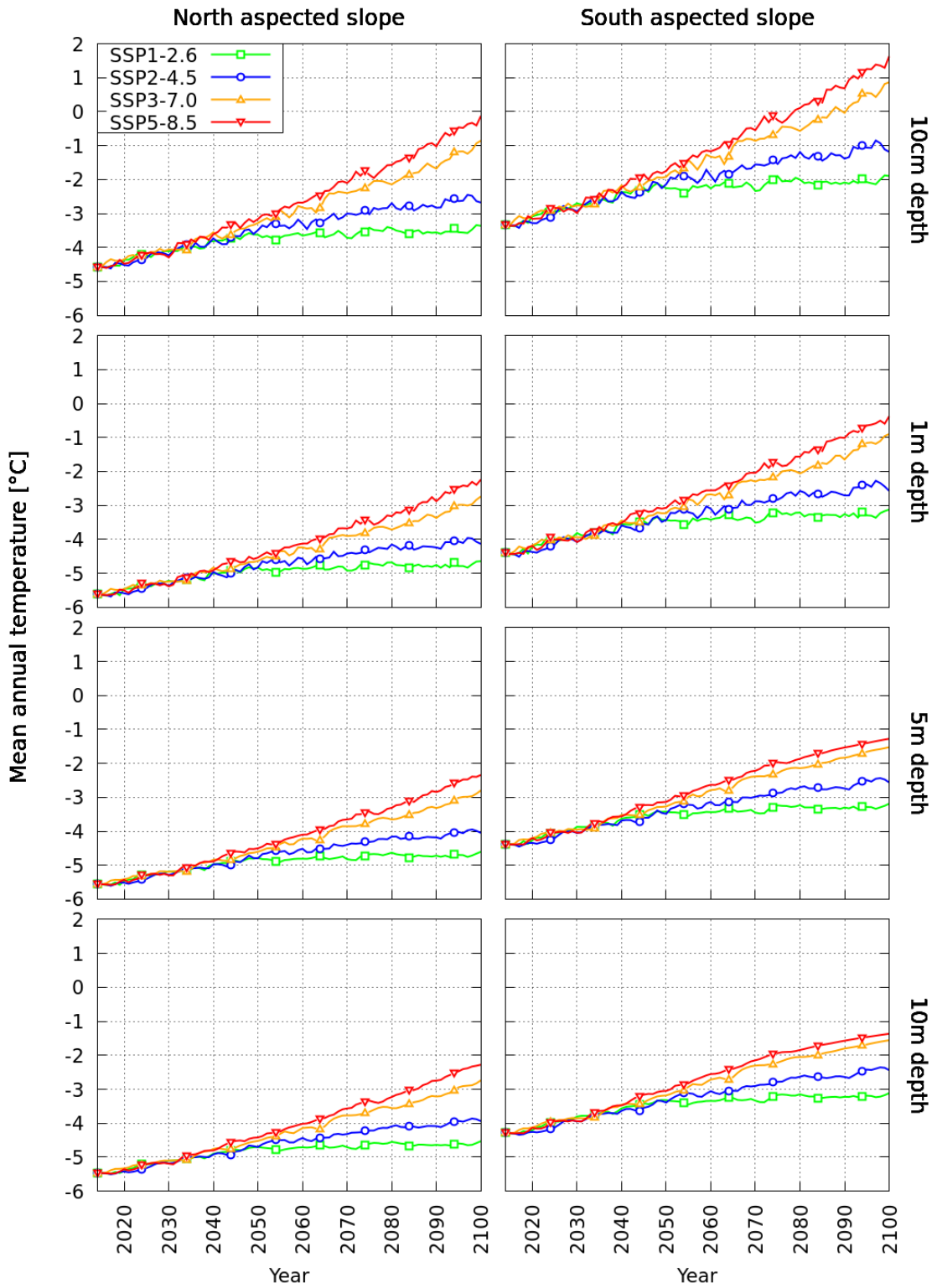
331 The four projections based on the different Shared Socioeconomics Pathways (SSPs)-scenarios lead
 332 to an increase of in the ground surface temperature from +1.4°C (SSP1-2.6) to +5.2°C (SSP5-8.5)
 333 between 2014 and 2100 (Fig. 5a and 5b). These rates of increase, roughly equivalent by
 334 extrapolation to +1.7°C/100 yrsyears (SSP1-2.6) and +5.9°C/100 yrsyears (SSP-8.5), are lower than
 335 the projected increases in air temperature (+1.9°C/100 yr years for SSP1-2.6 and +7.8°C/100 yryears
 336 for SSP5-8.5) due to the insulating effect of the snow cover and the vegetation layer, and also due to
 337 the thermal inertia of the soil column below the surface. One can note that for the SSP3-7.0 and
 338 SSP5-8.5 scenarios, the mean annual soil surface temperature becomes positive around 2080.

339 3.2 Trends in soil temperatures

340 The sSoil temperature at different depths is one of the key variables for characterizsing
 341 permafrost dynamics. The multi-annual trends induced by the climate warming of the mean annual
 342 soil temperature between 2014 and 2100 at 3four depths (10 cm, 1 m and 5 m and 10 m below the
 343 surface) are illustrated in Figure 6.

344

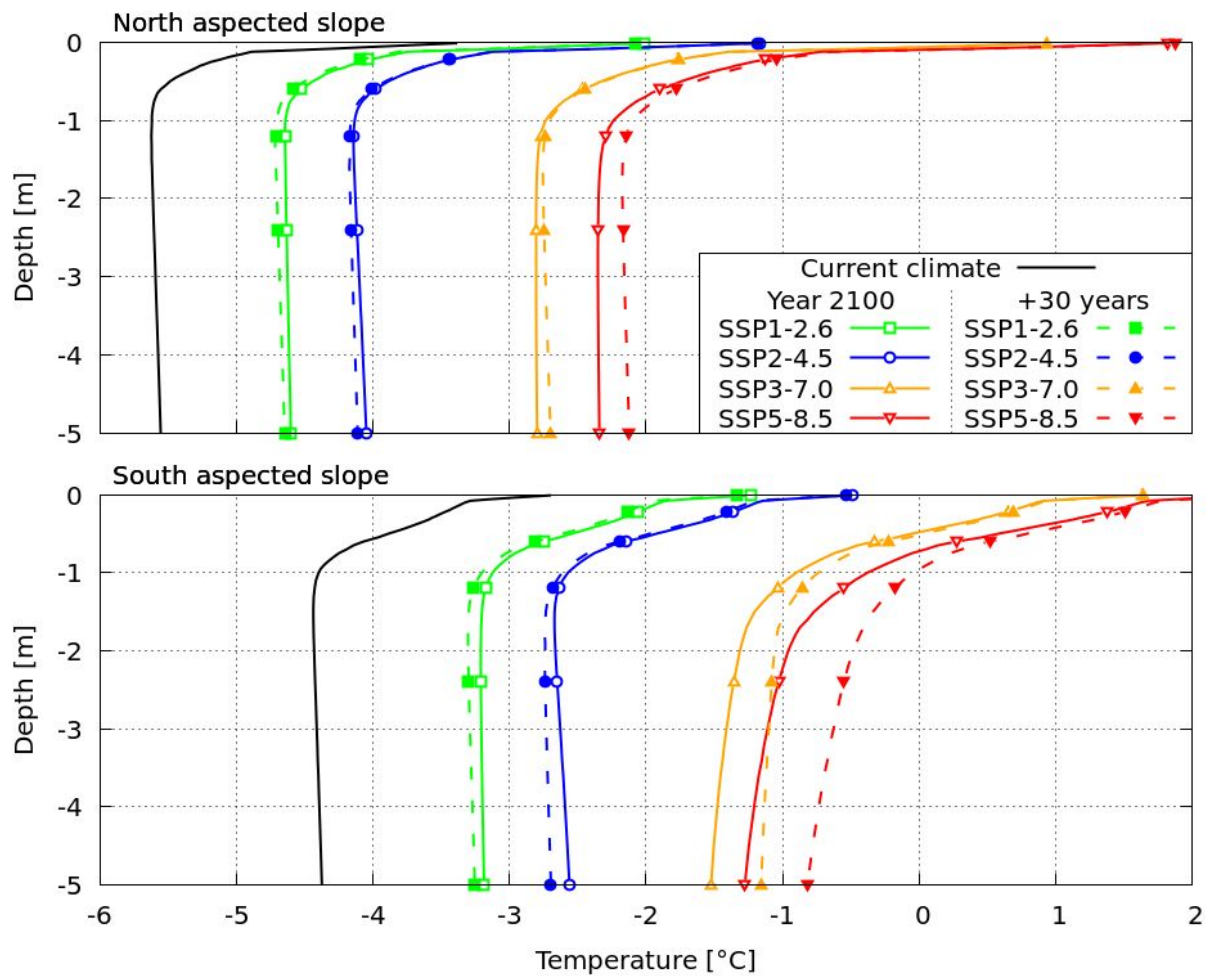
345



346

347 **Figure 6: Mean annual temperature evolution at 10 cm, 1 m, 5 m and 10 m under the surface**
 348 **for each scenario and slope considered.**

349 | ~~In~~On both slopes, the soil temperature experiences a significant increase down to 10 m
350 | depth, for all climate warming scenarios considered. The annual mean soil temperature even
351 | becomes ~~even~~-positive close to the surface (10 cm depth) in the SAS for the two ~~most~~-high-
352 | ~~end~~forcing pathway (hottest) scenarios, by 2080 ~~with-for~~ SSP5-8.5 and by 2090 ~~with-for~~ SSP3-7.0.
353 | Meanwhile, for the medium scenario SSP2-4.5 and for the low-forcing sustainable pathway
354 | (coldest) scenario SSP1-2.6, the mean annual soil temperature stays ~~s=~~everywhere negative
355 | everywhere until 2100. The warming is more intensive in the SAS than in the NAS, and, as
356 | expected, the amplitude of soil warming decreases with depth. In the SAS, at 10 cm depth the
357 | temperature rise between current conditions and the year 2100 is 1.4 °C for the SSP1-2.6 scenario
358 | and 5.0 °C for the SSP5-8.5 scenario, while at 5 m depth, the temperature rises are 1.2°C and 3.1
359 | °C, respectively. In the NAS, at 10 cm depth the temperature rise between current conditions and
360 | the year 2100 is ~~of~~-1.2-°C for the SSP1-2.6 scenario and ~~of~~ 4.4-°C for the SSP5-8.5 scenario, while
361 | at 5 m depth, the temperature rises are 1.0°C and 3.2°C, respectively. It should be noted that, for
362 | both slopes, the vertical gradient of the temperature in 2100 is higher in scenario SSP5-8.5 than in
363 | scenario SSP1-2.6. This indicates a stronger thermal non-equilibrium under more intense warming.
364 | For instance, the difference ~~of~~in temperature in 2100 between 10 cm depth and 5 m depth is 3.0-°C
365 | in the SAS and ~~of~~-2.2 °C in the NAS for scenario SSP5-8.5, while it is 1.3-°C in the SAS and 1.2°C
366 | in the NAS for the SSP1-2.6 scenario. In order to provide insight into the thermal equilibrium state
367 | of the soil columns in each slope in 2100, additional simulations have been performed by applying
368 | the projected climatic conditions of the end of the century (averaged over 2096–2100) for 30 more
369 | years. Then, fFor each scenario, the vertical soil temperature profiles for 2100 and for the numerical
370 | experiments with 30 more years of 2096–2100 climatic conditions are plotted in Figure 7.



371

372 **Figure 7: Annual mean temperature profiles in 2100 and after 30 years of additional cycling**
 373 **of the average climatic forcing between 2096 and 2100.**

374

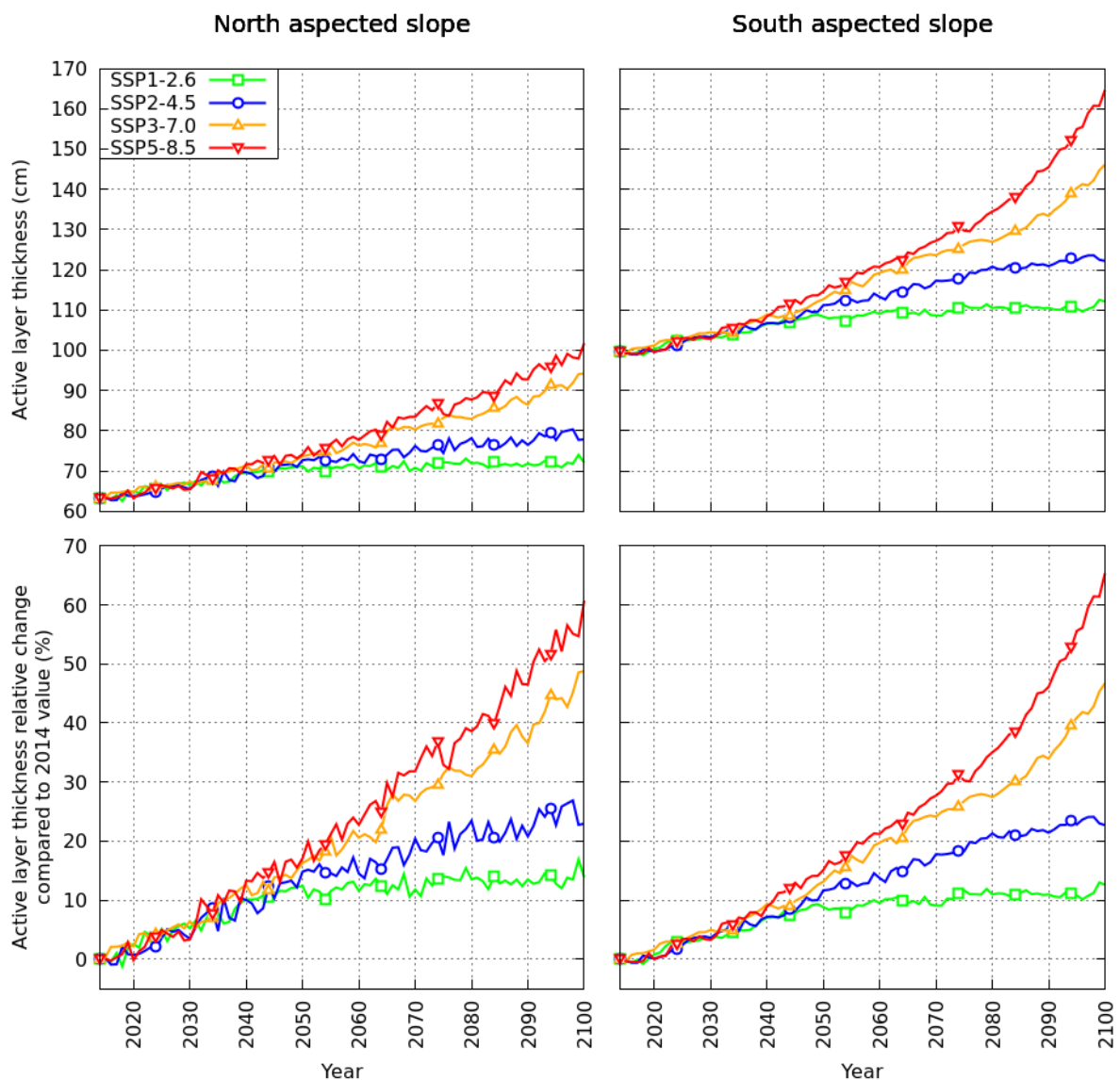
375 Considering the soil temperature profiles in 2100, two regions may be distinguished: the
 376 first metre, with steep positive vertical gradients (the soil surface is warmer than the bottom of the
 377 active layer), and a deeper region, with smoother vertical thermal gradients that are either slightly
 378 negative (SSP1-2.6 and SSP2-4.5 in the NAS and SAS), almost nil (SSP3-7.0 and SSP5-8.5 in the
 379 NAS) or positive (SSP3-7.0 and SSP5-8.5 in the SAS). -When comparing these profiles with those
 380 obtained with 30 additional years of modelling in constant '2096--2100' climatic conditions, we
 381 observe important differences in both slopes for scenario SSP5-8.5, and also for scenario SSP3-7.0
 382 and scenario SSP2-4.5, in the SAS.

383

384 **3.3 Active layer thickness evolution**

385 Numerical simulations give provide access to the soil temperature at various depths. From
 386 the soil temperature profile, the maximum depth with a positive temperature may be computed at
 387 each time step. The maximum thawed depth obtained over a year defines the active layer thickness
 388 (ALT) of this year. The aActive layer thickness has been computed for each scenario and each year
 389 and is plotted for both the NAS and SAS in Figure 8.

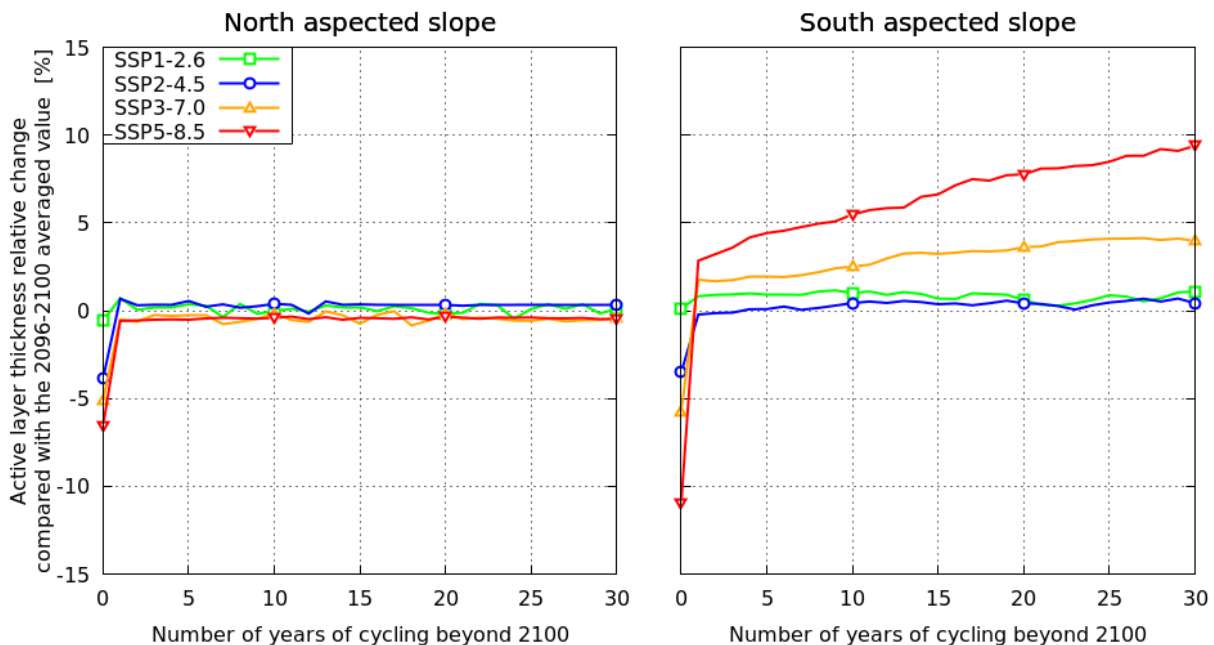
390



391 **Figure 8: Active layer thickness temporal evolution on theNorth-NAS (left) and South-SAS**
 392 **(right) aspect Slope of the Kulingdakan watershed obtained from permaFoam simulations**
 393 **under different SSP scenarios. Top : Active layer thickness value. Bottom : Relative change**
 394 **compared to 2014 value (63 cm for NAS, 100 cm for SAS).**

397 For both slopes, an increase in the active layer thickness is observed between 2014 and 2100 in
 398 every scenario, with a more important thickening in the SAS than in the NAS. SSP1-2.6 leads to an
 399 increase of +12.5 cm / +13% for the SAS and of +8.8 cm / +14% for the NAS, while SSP5-8.5
 400 leads to a more dramatic increase of +65.1 cm / +65% for the SAS and of +38.5 cm / +61% for the
 401 NAS. In the first half of the century, the behaviour of the active layer thickness does not differ
 402 significantly between scenarios, with a thickening rate in the ALT of about +3.6 mm/year ($\pm 23\%$)
 403 in the SAS and of +2.8 mm/year ($\pm 18\%$) in the NAS. However, in the second half of the century
 404 (2050–2100), different scenarios lead to very different active layer thickness evolution dynamics.
 405 For SSP1-2.6, the thickening rate is rather small, with a rate of +0.60 mm/year for the SAS and
 406 +0.32 mm/year for the NAS, while for the SSP5-8.5 scenario, the thickening rate rises to +9.1
 407 mm/year for the SAS and +5.1 mm/year for the NAS. By the end of the simulated period, these
 408 thickening rates show no diminishing trend in the SAS, suggesting that the dynamic thermal
 409 equilibrium is not reached in the active layer. For To illustrating this, Figure 9 shows the active
 410 layer thickness evolution for 30 years of additional simulations while keeping the climatic
 411 conditions of the end of the century (2096–2100) for each scenario.

412



413

414 **Figure 9: Relative change in active layer thickness compared with the average value averaged**
 415 **on for 2096–2100 over 30 years of spin-up on for a synthetic year obtained by averaging**
 416 **climatic conditions between 2096 and 2100.**

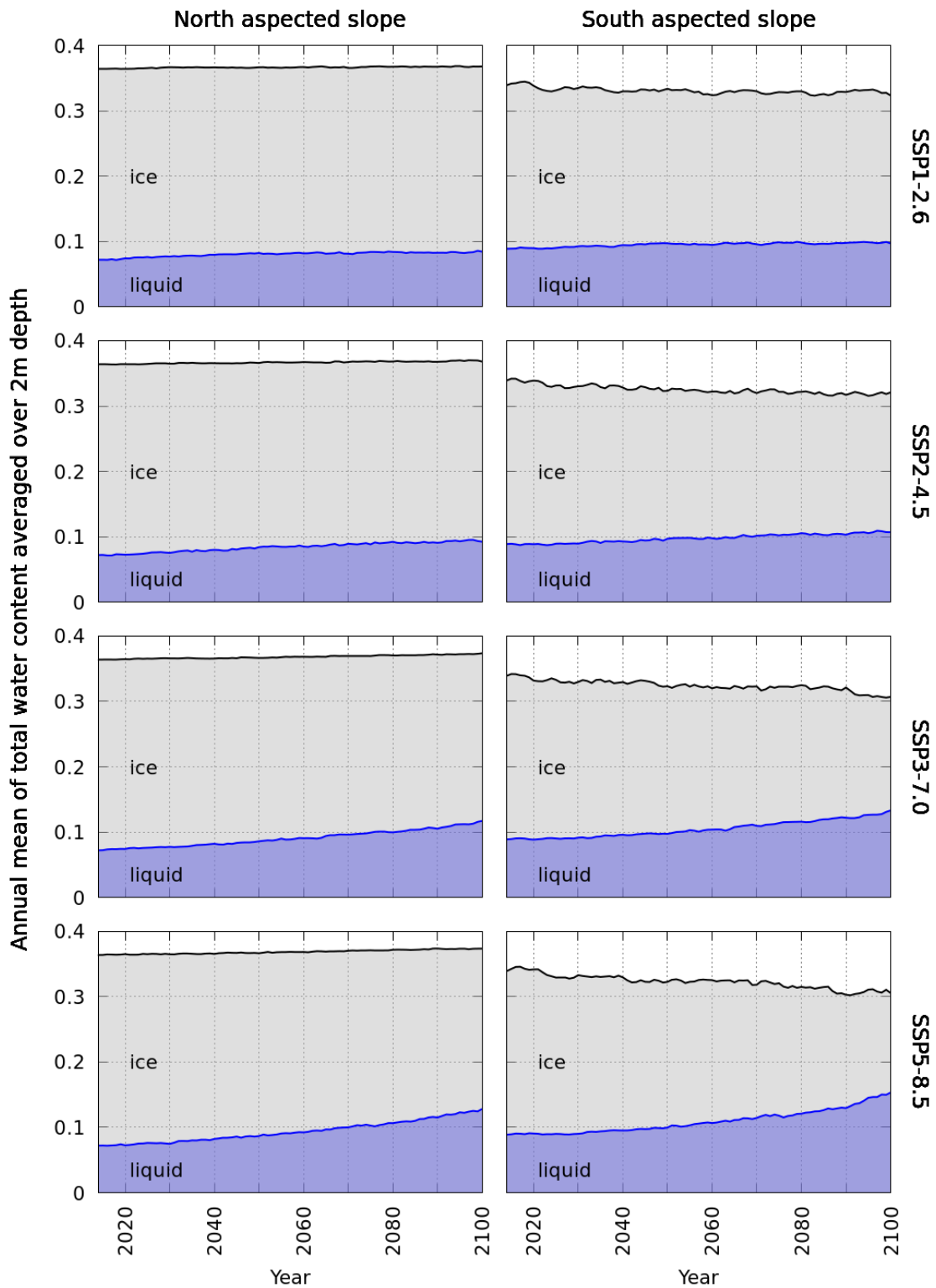
417

418 Overall, the active layer is not far from thermal equilibrium ~~in~~ on both slopes for the low-forcing
419 sustainable pathway (SSP1-2.6) and medium (SSP2-4.5) climatic scenarios. However, when
420 considering the high-end-forcing pathway SSP5-8.5 scenario, an important thermal inertia effect
421 appears in the SAS, with an additional active layer thickness increase over these 30 years of +10.4
422 % compared to the 2096–2100 value, i.e. an increase of +17 cm. This additional change in the
423 active layer thickness brings the resulting change compared to the 2014 value to +77 cm (+77%) for
424 the SSP5-8.5 scenario for the SAS. The abrupt change observed at the end of the first year of
425 cycling is a direct observation of the abrupt change ~~of~~ in climatic forcing (from 2100 forcings to
426 2096–2100 averaged conditions). Interannual variability is included in CMIP6 scenarios, as ~~it~~
427 can be seen in Figure 2 for both the air temperature and precipitations. For the NAS, the active layer is
428 back to equilibrium in a year, which is a sign of a short response time. For the SAS, and particularly
429 for the steepest scenarios, this effect is added to a longer response time change, as discussed
430 previously.

431 3.4 Trends in soil moisture

432 The soil moisture content experienced less important changes than the thermal regime
433 under the considered climate change scenario. ~~For To~~ illustrating the soil moisture evolution near
434 the surface, the total water, liquid water and ice volumetric contents have been averaged over the
435 first 2 m of the soil for each slopes, and their 2014–2100 evolutions have been plotted in Figure
436 10 for the four climatic scenarios. Note that the 2 m surface soil layer thickness considered for this
437 quantification encompasses the entire area with water content evolution under the climate change
438 scenarios. Regardless of the scenario, there is no significant evolution of the total water content in
439 the first two meters of soil in the NAS, and the only noticeable change is the increase in the
440 proportion of liquid water (+17% in SSP1-2.6, +28 % in SSP2-4.5, +62% in SSP3-7.0, +78% in
441 SSP5-8.5), suggesting an increase in the amount of liquid water available for vegetation. In the
442 SAS, however, the first two meters of the soil exhibited a slight but detectable diminishing of the
443 total water content by 2100 (-5 % in SSP1-2.6 and SSP2-4.5, -10% in SSP3-7.0 and SSP5-8.5). On
444 the other hand, the proportion of liquid water over ice increases (+9% in SSP1-2.6, +20% in SSP2-
445 4.5, +50% in SSP3-7.0, +72% in SSP5-8.5). Therefore, on the SAS-slope, climate warming may
446 result in an increase ~~of~~ in the amount of liquid water available for vegetation. This finding is
447 important for heat and water transfers in the soil, given the strong couplings and non-linearities
448 between these transfers. For instance, decreasing the total water content induces a decrease in the

449 | soil thermal inertia, while decreasing the share of ice versus liquid water induces a decrease in the
450 | apparent thermal conductivity. This can also impact the vegetation dynamics, since vegetation takes
451 | up only liquid soil water for transpiration. It should be emphasized that the presented partitioning
452 | between liquid water and ice is based on the mean annual quantities. This provides a considerably
453 | smaller proportion of liquid water compared to that at ~~in~~ the end of the active season (second half of
454 | September), when the active layer is at its maximum thickness.

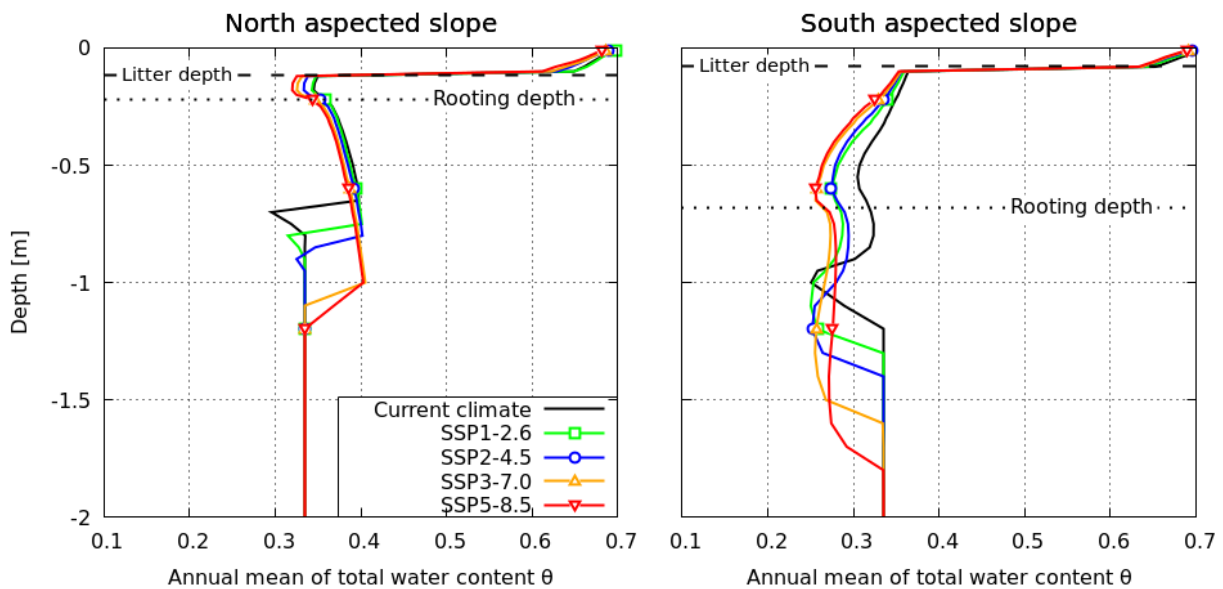


455

456 **Figure 10: Annual mean of total water content [m³ of water / m³ of soil], liquid water content**
 457 **and ice content averaged over 2m depth in different climate projections.**

458

459 In order to investigate the local variation of the moisture content in the rooting zone and in
 460 the active layers of each slopes, the vertical profiles of the mean annual total water content have
 461 been plotted oin Figure 11 for current climatic conditions and for the year 2100 under the SSP1-2.6,
 462 SSP2-4.5, SSP3-7.0 and SSP5-8.5 scenarios. The processes driving the evolution of vertical
 463 moisture profiles are complex; ~~that~~they involve coupled and non-linear heat and water transfers, as
 464 well as changing evapotranspiration fluxes. The relevant changes oin the vertical moisture profiles
 465 can be described as followings. The water profiles do not change significantly in the highly porous
 466 organic horizon infor both slopes. In the mineral horizon, the behaviours of the SAS and NAS get
 467 ~~more~~-contrast moreed, due to downward vertical moisture gradients (and thus, according to the
 468 generalized Darcy's law, upward water movements) in the NAS and upward vertical moisture
 469 gradients (and thus downward water movements) in the SAS. In the NAS, the only evolution with
 470 climate change is a thickening of the zone with a downward vertical moisture gradient (i.e.; an
 471 upward water flux) alongside the thickening of the active layer, with no significant changes oin the
 472 gradient itself. Meanwhile, in the SAS, alongside with the thickening of the zone with water
 473 movements (i.e. moisture gradients) that comes with active layer thickening, significant changes
 474 oin the upward moisture gradients are expected to occur: the hotter the scenario, the steeper the
 475 gradients, and thus the stronger the downward water fluxes.



476
 477 **Figure 11: 2-Two-metre -depth profiles of the annual mean of the total water content [m³ of**
 478 **water / m³ of soil] in 2100: projections compared to current state.**

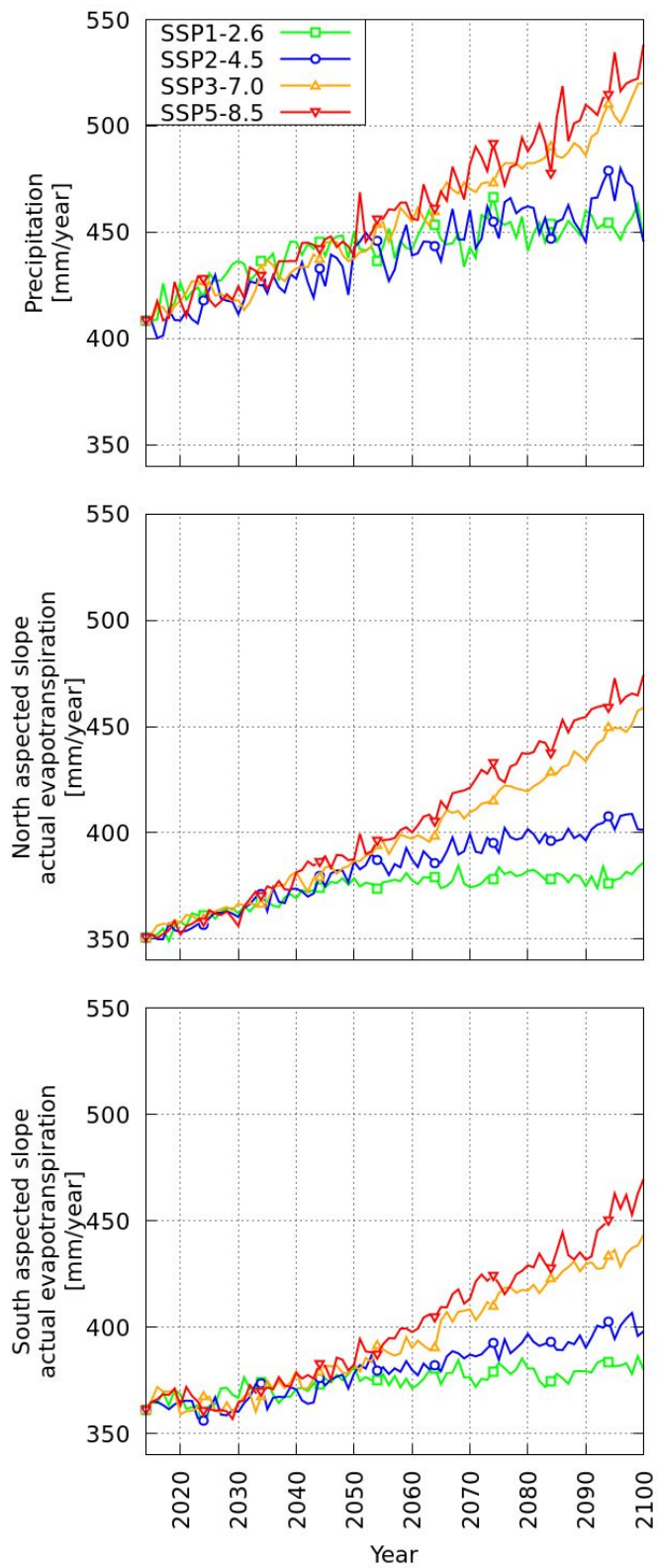
479

480 3.5 Water fluxes

481 | The water fluxes also significantly change ~~along~~ with climate change ~~in~~ on both slopes for
482 every scenario. Evapotranspiration is the most important component of the hydrological budget in
483 Kulingdakan. Focusing on this dominant component, Figure 12 presents the centennial evolution of
484 evapotranspiration ~~in~~ on both slopes and ~~of~~ precipitation for the four climate change scenarios. A
485 significant increase ~~in~~ ~~of~~ evapotranspiration is simulated in all cases, with an increase between +19
486 mm / +5% (SSP1-2.6) and +108 mm / +30% (SSP5-8.5) in ~~the~~ SAS, and between +35mm / +10%
487 and +123 mm / +35% in ~~the~~ NAS. The increase in the evapotranspiration fluxes in Kulingdakan
488 ~~are~~ is correlated to the increase in precipitation, with similar rates for both slopes.

489

490



491

492 **Figure 12: Precipitation and actual evapotranspiration evolution over the century**

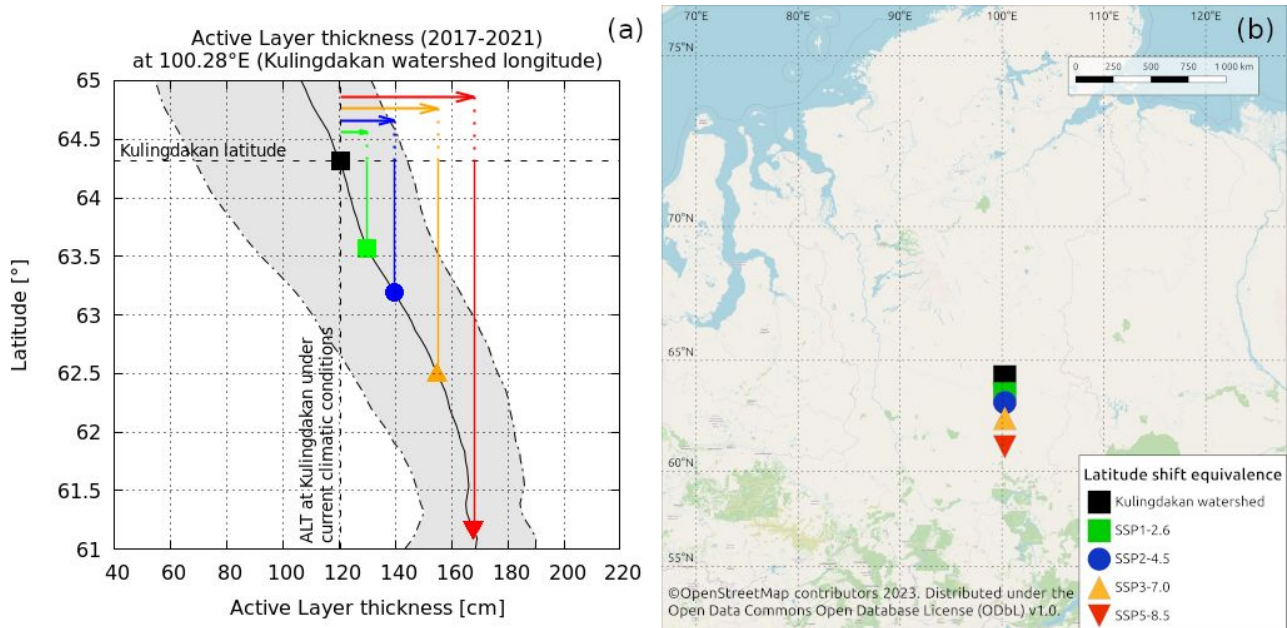
493 Similar to previous simulations of Mean Annual Temperature, soil surface temperature and Active
494 Layer Thickness, the evolution is globally similar among scenarios until 2050, with significant
495 divergences appearing only between 2050 and 2100.

496 4 Discussion

497 | The numerical results obtained by the mechanistic modelling of heat and water transfer
498 | within the permafrost and active layer of Kulingdakan document the physical response to be
499 | expected within this catchment under climate change, with soil warming (Figure, 6) and active layer
500 | thickening (Figure, 8) in all climate scenarios. An important spatial variability of this thermal
501 | response is identified, in relation with the aspect of the slopes, which stems from a sizable contrast
502 | in the vegetation cover, hydrologic and thermal state and active layer dynamics, as currently
503 | observed between the two slopes of the catchment (Prokushkin et al., 2007). Indeed, since the NAS
504 | is wetter, its thermal inertia is more important due to the larger amount of latent heat that must be
505 | provided in order to thaw and warm its soils, compared to the drier soils of the SAS. This difference
506 | in moisture content is largely due to the differences in the tree cover biomass and physiology. In
507 | particular, the deeper root layer in the SAS compared to the NAS induces more intensive
508 | evapotranspiration, both under both current (Orgogozo et al., 2019) and future climate conditions.
509 | Note that this contrast between the two slopes tends to diminish with climate warming (Figure, 12),
510 | although the SAS will always remain drier than the NAS (Figure 10). The pattern of water fluxes
511 | within the active layer, with an upward flux to the thinner, close-to-the-surface root layer in the
512 | NAS and a downward flux toward the bottom of the thicker root layer in the SAS is also preserved
513 | under climate change, with an intensification of the fluxes in the SAS under the high-end-forcing
514 | pathway scenarios (Figure 11). Furthermore, the thicker moss layer in the NAS is likely to alleviate
515 | more efficiently the effect of changes in the climatic conditions on soil compared to that in the SAS.
516 | Because our modelling takes into account the root water uptake mechanistically (Orgogozo et al.,
517 | 2023) and the low vegetation insulating effect empirically (Supplementary mMaterial A), the
518 | warming of the soil and the thickening of the active layer under climate change are significantly
519 | more pronounced in the SAS than in the NAS. This spatial variability in permafrost dynamics of
520 | forest environments, persistent at all climate change scenarios, reflects the prominent role of micro-
521 | climatic conditions in the responses to climate change that has been demonstrated recently in the
522 | literature (Zellweger et al., 2020).- It must be emphasized that all the numerical results of this study
523 | have been obtained considering the vegetation in its present state. The Sstrong local variabilities of
524 | the vegetation cover depending on the permafrost conditions in the Kulingdakan catchment
525 | (Orgogozo et al., 2019) and, in from a broader perspective, in the entire-Arctic (Oehri et al., 2022),
526 | are consistent with the tight connections between the evolution of vegetation evolution-under

527 | climate change (e.g. Vitasse et al. 2009, 2011; Rew et al., 2020) and the permafrost pattern, which
528 | has not been explicitly considered in this study. At the centennial time scale, changes in the tree
529 | growth rate, the forest fire frequency or the nature of the vegetation cover may exert important
530 | impacts on permafrost conditions (Cable et al., 2016; Fedorov et al., 2019; Rew et al., 2020; Li et
531 | al., 2021; Heijmans et al., 2022). -Meanwhile, without belittling these complex interactions between
532 | vegetation and permafrost dynamics, this study shows that important impacts of climate change ~~are~~
533 | ~~to be expected~~ on the permafrost dynamics of the forested continuous permafrost area are to be
534 | expected, even withat the steady state of the vegetation. We noted that the more intense the climate
535 | change, the more pronounced these thermal responses. For instance, under the SSP5-8.5 scenario, a
536 | maximum evolution of the active layer thickness is $+65\text{ cm}_/_+65\%$ for the SAS and $+39\text{ cm}_/_$
537 | $+61\%$ for the NAS, while in the SSP2-4.5 scenario, an increase of $+23\text{ cm}_/_+23\%$ for the SAS and
538 | of $+15\text{ cm}_/_+23\%$ for the NAS is anticipated. Using empirical transfer functions to approximate for
539 | approximating the soil surface temperature from atmospheric conditions under climate change
540 | poses the problem of extrapolation, for instance under extreme hot weather conditions that may
541 | occur in the future, which are being unprecedented in the training period 1999–2014. However,
542 | performing the mechanistic modelling of the surface energy balance in extreme weather conditions
543 | under permafrost contexts was beyond the scope of this work. Besides/Additionally, it must be noted
544 | that for now in permaFoam, evapotranspiration is assumed to be solely constituted by transpiration,
545 | while the evaporation within the soil is neglected (Orgogozo et al., 2019). This assumption is made
546 | in the context of the study of boreal forest areas, in which transpiration largely dominates over
547 | evaporation in the hydrological budget (e.g.; Park et al., 2021). Meanwhile, evaporation may
548 | dominate in tundra environments (Clark et al., 2023); and likely to increase in the future in forested
549 | environments. Since soil evaporation adds another coupling between heat and water transfers
550 | through exchanges of latent heat, it could directly affect the soil temperature evolution. These points
551 | should constitute a scope of future modelling works.

552 | To produce a broader geographical context of the active layer thickening projections
553 | simulated at the scale of a small catchment, a comparison of centennial evolutions under climate
554 | change with large geographical coverage is performed using a substituting space for time approach
555 | (Fig. 13).



556

557 **Figure 13: (a) Equivalence between simulated active layer thickening by 2096–2100 under**
 558 **climate change (SAS and NAS average) and southward latitudinal shift in current climatic**
 559 **conditions (2017–2021). — Hlatitudinal trend (black line — average over a 1°lat. × 1°long.**
 560 **polygon) and envelope (in grey — min./max. over years within the same polygon) extracted**
 561 **from Permafrost CCI (Westermann et al., 2024). (b) Representation of the latitudinal**
 562 **southward shift equivalent to each climate scenario’s active layer thickening on the regional**
 563 **map.**

564

565 The simulated thickening of the active layer, averaged over both slopes of Kulingdakan, ~~are~~
 566 depicted as southward latitudinal shifts along the meridian passing by Kulingdakan, i.e. with a
 567 ~~N~~North-~~S~~South translation along ~~the~~ 100.28 °E (Fig. 13). The latitudinal evolution of the active layer
 568 thickness along the current meridian is computed based on the permafrost_CCI dataset
 569 (Westermann et al., 2024); by averaging the value of the multi-annual mean of ~~the~~ active layer
 570 thickness for the 2017–2021 period over a polygon of 1° ~~of~~ latitude by 1° of longitude centered
 571 on the considered meridian and browsing the latitude between 67°N and 57°N. **The 1°-1° polygon was**
 572 **considered big enough to smooth the small-scale non-homogeneities (at km scale) and small enough**
 573 **to capture the latitudinal effect, including biome transitions (~hundreds of km, e.g.: Anisimov et al.,**
 574 **2015) In Figure 13(a), the black line describes the multi-annual (1997–2019) temporal average of**
 575 **the spatial average of the active layer thickness over a 1°-1° polygon centered on a moving latitude ;**
 576 **the grey shaded area represents the minimum/maximum obtained for this spatial average during**
 577 **the considered period.** It can be seen that, in the **high-end-forcing pathway** scenario SSP5-8.5, the

578 active layer thickening would correspond to a 349 km southward shift, while in the medium
579 scenario SSP2-4.5, it would correspond to a 124 km southward shift.

580 Under a permanently changing climatic context, an important question is the state of thermal
581 equilibrium versus non-equilibrium of the permafrost (Obu et al., 2019): is the climate change
582 induced warming slow enough ~~so~~ that permafrost may be considered at every time close to the
583 thermal equilibrium with climatic conditions, or on the contrary, do the transient effects dominate
584 the thermal dynamics of permafrost under climate change? The simulation results of this work
585 provide information for characterizing the degree of thermal equilibrium of the continuous
586 permafrost, in a forested study site under various scenarios of climate change. First of all, we
587 emphasize that, since the bottom thermal boundary condition in our modelling is the geothermal
588 heat flux (Duchkov et al., 1997), the assumption of overall thermal equilibrium ~~in~~at depth (<-10 m)
589 in the hundreds of ~~metres~~ of the thick permafrost of the Putorana plateau (Pokrovsky et al., 2005)
590 is implicitly made. Meanwhile, the temperature profiles shown in Figure 7 demonstrate that under
591 this assumption the thermal equilibrium state of the first 10 m of soil in 2100 depends on both the
592 climate change scenario and the slope aspect. In the NAS, the thermal equilibrium of the first 10 m
593 of soil is achieved by 2100 in every climate scenario, with only a slight shift between the 2100 and
594 (2100+30) conditions in the SSP5-8.5 scenario. ~~Additionally~~Besides, with sub-zero vertical
595 thermal gradients in each scenario, only small heat exchanges between the surface and the deep
596 layer may occur. On the contrary, by 2100 ~~—~~in the SAS, strong thermal non-equilibrium is
597 encountered in the two high-end-forcing pathway scenarios, SSP3-7.0 and SSP5-8.5 (Figures, 7
598 and 8). Under these scenarios, sizable evolutions of temperature profiles are expected between 2100
599 and 2100+30. Moreover, for these two scenarios, the vertical thermal gradients between 1 and 10 m
600 depth are clearly positive (considering an upward vertical axis), which implies an ongoing heat flux
601 from the surface to the depths. In this case, the permafrost is warming below 10 m, at a rate that we
602 implicitly assume to be small enough ~~so~~ that it does not modify the total amount of heat stored
603 within this deep permafrost. As such, in scenarios SSP3-7.0 and SSP5-8.5, the climate change
604 clearly induces the transient warming of the permafrost below 10 m depth in the ~~south-aspect~~
605 slopesSAS of the Kulingdakan watershed. One could note ~~a~~ slightly decreasing trends in the soil
606 temperature under scenarios SSP1-2.6 and SSP2-4.5. This is due to inter-annual variabilities in both
607 the precipitation and air temperature in CMIP6 projections (Figure, 2). Therefore, the year 2100;
608 ~~which is repeated over 30 cycles to assess the equilibrium state of the permafrost,~~
609 different conditions from those observed in the ~~previous decade 2090-2100~~2096-2100 average.

610 | which is repeated over 30 cycles to assess the equilibrium state of the permafrost. For example, in
611 | SSP2-4.5, the last decade experiences an important annual precipitation peak, up to 475 mm/year,
612 | centered around 2095, before a decreasing trend ~~on~~in the second part of the decade, ending up
613 | ~~to~~with a precipitation of 410 mm/year projected in 2100. This results, for the year 2100, in a
614 | decrease ~~of~~in the snow cover insulating effect in winter; and thus a ~~cooling~~-lowering of the soil
615 | surface temperature (Fig. 5), compared to the conditions encountered in the previous decade.

616 | Overall, the results of the present study may be used to improve our understanding of the
617 | climate-~~w~~warming-related changes in the wide areas of boreal forest on continuous permafrost, with
618 | implications for continental surfaces (Revich et al., 2022), ecosystems (Wang and Liu 2022) and
619 | element cycles (Schuur et al., 2022), and related global consequences and feedbacks. ~~The use of m~~
620 | Mechanistic modelling, although it is computationally costly, is capable of providing quantitative
621 | information for ~~feeding~~these research fields. This approach should be applied in other
622 | environmentally monitored boreal watershed, in order to numerically characterize the physical
623 | response of permafrost to climate change under various environmental contexts, for instance, in
624 | Northern Sweden (Auda et al., 2023) and Western Siberia (Cazaurang et al., 2023).

625 | 5 Conclusion

626 | Four main conclusions that could be drawn from this numerical study are the following:

- 627 | - All climate change scenarios trigger significant soil warming (+1.8°C in the SAS and +1.5°C in
628 | the NAS under the SSP2-4.5 scenario at 1 meter depth according to the presented simulations) and
629 | an increase in the active layers thickness (+23 cm / +23% in the SAS and +15 cm / +23% in the
630 | NAS under the SSP2-4.5 scenario) ~~in~~for both slopes of the Kulingdakan watershed. The projected
631 | increase of in the active layer thickness under the SSP2-4.5 scenario would be equivalent to a ~120
632 | km southward shift in current climatic conditions, and to a ~350 km southward shift under the
633 | SSP5-8.5 scenario.
- 634 | - For all climate change scenarios, the combination of soil warming and an increase in precipitation
635 | ~~increase~~leads to an important increase in evapotranspiration ~~in~~for both slopes (+37 mm / +10% in
636 | the SAS and +51 mm / +14% in the NAS under the SSP2-4.5 scenario). Meanwhile, the mean
637 | annual soil moisture decreases only slightly in the NAS (-2.3% under the SSP2-4.5 scenario,
638 | averaged over the 22 cm of rooting depth), but the decrease is more pronounced in the SAS (-6.0%
639 | ~~in NAS~~ under the SSP2-4.5 scenario, averaged over the 68 cm of rooting depth).

640 | - The ~~h~~important spatial variability observed in the Kulingdakan watershed illustrate the key role of
641 | meso-climatic conditions and small-scale geomorphological contrasts in the permafrost response to
642 | climate warming

643 | - Under the two high-end-forcing pathway scenarios of climate change, SSP3-7.0 and SSP5-8.5,
644 | the near-surface permafrost of the SAS of the Kulingdakan watershed are-is in a non-equilibrium
645 | thermal state in 2100, and further investigation is needed to assess whether or not the permafrost
646 | underneath-below 10 m depth will be close to thermal equilibrium in this region. This advocates
647 | indicates the need of-to developing non-equilibrium modelling approaches for regional and global
648 | permafrost modelling under climate change.

649 | The approach developed in this study can be applied to other high-latitude permafrost-affected
650 | catchments, provided that the necessary informations on current thermal and hydrological
651 | parameters of the soil as well as vegetation coverage, are-is available.

652

653 | **Competing interests**

654 | The contactcorresponding author has declared that none of the authors has any competing interests.

655 | **Acknowledgments**

656 | This work has been funded by the French National Research Agency ANR (grant n^o ANR-19
657 | CE46-0003-01); and benefited from access to the supercomputers of CALMIP (project p12166) and
658 | GENCI (project A0140410794, TGCC). This work was supported by a French government grant
659 | managed by the Agence Nationale de la Recherche under the "Investissements d'avenir" program
660 | (reference "ANR-21-ESRE-0051"). Oleg Pokrovsky is grateful for partial support from the TSU
661 | Development Programme PRIORITY – 2030 and project PEACE of PEPR FairCarboN ANR-22-
662 | PEXF-0011. Anatoly Prokushkin is supported by State Assignment no. 0287-2021-0008. Esteban
663 | Alonso Gonzalez is supported by the European Space Agency through the Climate Change
664 | Initiative postdoctoral grant.

665 **References**

666 Alonso-González, E., Aalstad, K., Baba, M. W., Revuelto, J., López-Moreno, J. I., Fiddes, J.,
667 Essery, R., and Gascoin, S.: The Multiple Snow Data Assimilation System (MuSA v1.0), *Geosci.*
668 *Model Dev.*, 15, 9127–9155, <https://doi.org/10.5194/gmd-15-9127-2022>, 2022.

669

670 Anisimov, O. A., Zhiltcova, Y. L., and Razzhivin, V. Y.: Predictive modeling of plant productivity
671 in the Russian Arctic using satellite data, *Izvestiya Atmospheric and Oceanic Physics*, 51(9), 1051–
672 1059, <https://doi.org/10.1134/S0001433815090042>, 2015.

673

674 Arndal, M. F., and Topp-Jørgensen, E. (Eds.): INTERACT Station Catalogue – 2020, DCE –
675 Danish Centre for Environment and Energy, Aarhus University, Denmark, 190 pp., ISBN 978-87-
676 93129-15-3, www.eu-interact.org, 2020.

677

678 Auda, Y., Lundin, E. J., Gustafsson, J., Pokrovsky, O. S., Cazaurang, S., and Orgogozo, L.: A new
679 land cover map of two watersheds under long-term environmental monitoring in the Swedish Arctic
680 using Sentinel-2 data, *Water*, 15, 3311, <https://doi.org/10.3390/w15183311>, 2023.

681

682 Bartsch, A., Pointner, G., Nitze, I., Efimova, A., Jakober, D., Ley, S., Högström, E., Grosse, G., and
683 Schweitzer, P.: Expanding infrastructure and growing anthropogenic impacts along Arctic coasts,
684 *Environ. Res. Lett.*, 16, 115013, <https://doi.org/10.1088/1748-9326/ac3176>, 2021.

685

686 Blok, D., Heijmans, M. M. P. D., Schaepman-Strub, G., Van Ruijven, F., Parmentier, F. J. W., and
687 Maximov, T. C.: The cooling capacity of mosses: Controls on water and energy fluxes in a Siberian
688 tundra site, *Ecosystems*, 14, 1055–1065, <https://doi.org/10.1007/s10021-011-9463-5>, 2011.

689

690 Braithwaite, R. J., and Olesen, O. B.: Calculation of glacier ablation from air temperature, West
691 Greenland, in: *Glacier Fluctuations and Climatic Change*, edited by: Oerlemans, J., Kluwer
692 Academic Publishers, 219–233, 1989.

693

694 Biskaborn, B. K., Smith, S. L., Noetzli, J., *et al.*: Permafrost is warming at a global scale, *Nat.*
695 *Commun.*, 10, 264, <https://doi.org/10.1038/s41467-018-08240-4>, 2019.

696

697 Cable, W. L., Romanovsky, V. E., and Jorgenson, M. T.: Scaling-up permafrost thermal
698 measurements in western Alaska using an ecotype approach, *The Cryosphere*, 10, 2517–2532,
699 <https://doi.org/10.5194/tc-10-2517-2016>, 2016.
700

701 Cazaurang, S., Marcoux, M., Pokrovsky, O. S., Loiko, S. V., Lim, A. G., Audry, S., Shirokova, L.
702 S., and Orgogozo, L.: Numerical assessment of morphological and hydraulic properties of moss,
703 lichen and peat from a permafrost peatland, *Hydrol. Earth Syst. Sci.*, 27, 431–451,
704 <https://doi.org/10.5194/hess-27-431-2023>, 2023.
705

706 **Clark, J. A., Tape, K. D., and Young-Robertson, J. M., Quantifying evapotranspiration from**
707 **dominant Arctic vegetation types using lysimeters, *Ecohydrology*, 16(1), e2484, 2023.**
708

709 De Vrese, P., Georgievski, G., Gonzalez Rouco, J. F., Notz, D., Stacke, T., Steinert, N. J.,
710 Wilkenskjeld, S., and Brovkin, V.: Representation of soil hydrology in permafrost regions may
711 explain large part of inter-model spread in simulated Arctic and subarctic climate, *The Cryosphere*,
712 17, 2095–2118, <https://doi.org/10.5194/tc-17-2095-2023>, 2023.
713

714 Dominé, F., Fourteau, K., Picard, G., *et al.*: Permafrost cooled in winter by thermal bridging
715 through snow-covered shrub branches, *Nat. Geosci.*, 15, 554–560, [https://doi.org/10.1038/s41561-](https://doi.org/10.1038/s41561-022-00979-2)
716 [022-00979-2](https://doi.org/10.1038/s41561-022-00979-2), 2022.
717

718 Duchkov, A. D., Sokolova, L. S., Balobaev, V. T., Devyatkin, V. N., Kononov, V. I., and Lysak, S.
719 V.: Heat flow and geothermal field in Siberia, *Geologiya / Geofizika*, 38(11), 1716–1729, 1997.
720

721 Essery, R.: A factorial snowpack model (FSM 1.0), *Geosci. Model Dev.*, 8, 3867–3876,
722 <https://doi.org/10.5194/gmd-8-3867-2015>, 2015.
723

724 Eyring, V., Bony, S., Meehl, G. A., Senior, C. A., Stevens, B., Stouffer, R. J., and Taylor, K. E.:
725 Overview of the Coupled Model Intercomparison Project Phase 6 (CMIP6) experimental design and
726 organization, *Geosci. Model Dev.*, 9, 1937–1958, <https://doi.org/10.5194/gmd-9-1937-2016>, 2016.
727

728 Fan, X., Duan, Q., Shen, C., Wu, Y., and Xing, C.: Global surface air temperatures in CMIP6:
729 Historical performance and future changes, *Environ. Res. Lett.*, 15, 104056,
730 <https://doi.org/10.1088/1748-9326/abb051>, 2020.

731

732 Fedorov, A. N., Konstantinov, P. Y., Vasilyev, N. F., and Shestakova, A. A., The influence of
733 boreal forest dynamics on the current state of permafrost in Central Yakutia, *Polar Science*, 22,
734 100483, <https://doi.org/10.1016/j.polar.2019.100483>, 2019.

735

736 Frolking, S.: Sensitivity of spruce/moss boreal forest net ecosystem productivity to seasonal
737 anomalies in weather, *Journal of Geophysical Research*, 102(D24), 29053–29064,
738 <https://doi.org/10.1029/96JD03707>, 1997.

739

740 Gauthier, S., *et al.*: Boreal forest health and global change, *Science*, 349, 819–822,
741 <https://doi.org/10.1126/science.aaa9092>, 2015.

742

743 Gentsch, N.: Permafrost Soils in Central Siberia: Landscape Controls on Soil Organic Carbon
744 Storage in a Light Taiga Biome, Akademische Verlagsgemeinschaft München, Munich, Germany,
745 2011.

746

747 Haesen, S., Lembrechts, J. J., De Frenne, P., Lenoir, J., Aalto, J., Ashcroft, M. B., Kopecký, M.,
748 Luoto, M., Maclean, I., Nijs, I., Niittynen, P., van den Hoogen, J., Arriga, N., Brúna, J., Buchmann,
749 N., Čiliak, M., Collalti, A., De Lombaerde, E., Descombes, P., ... Van Meerbeek, K.: ForestTemp –
750 Sub-canopy microclimate temperatures of European forests, *Global Change Biology*, 27, 6307–
751 6319, <https://doi.org/10.1111/gcb.15892>, 2021.

752

753 Hamm, A., and Frampton, A.: Impact of lateral groundwater flow on hydrothermal conditions of the
754 active layer in a high-Arctic hillslope setting, *The Cryosphere*, 15, 4853–4871,
755 <https://doi.org/10.5194/tc-15-4853-2021>, 2021.

756

757 Hamon, W.R.: Computation of direct runoff amounts from storm rainfall, *International Association*
758 *of Scientific Hydrological Sciences Publication*, 63, 52–62, 1963.

759

760 Heijmans, M. M. P. D., Magnússon, R. Í. Lara, M. J., *et al.*: Tundra vegetation change and impacts
761 on permafrost, *Nat. Rev. Earth Environ.*, 3, 68–84, <https://doi.org/10.1038/s43017-021-00233-0>,
762 2022.

763

764 Hersbach, H., Bell, B., Berrisford, P., Hirahara, S., Horányi, A., Muñoz-Sabater, J., Nicolas, J.,
765 Peubey, C., Radu, R., Schepers, D., Simmons, A., Soci, C., Abdalla, S., Abellan, X., Balsamo, G.,
766 Bechtold, P., Biavati, G., Bidlot, J., Bonavita, M., De Chiara, G., Dahlgren, P., Dee, D.,
767 Diamantakis, M., Dragani, R., Flemming, J., Forbes, R., Fuentes, M., Geer, A., Haimberger, L.,
768 Healy, S., Hogan, R. J., Hólm, E., Janisková, M., Keeley, S., Laloyaux, P., Lopez, P., Lupu, C.,
769 Radnoti, G., de Rosnay, P., Rozum, I., Vamborg, F., Villaume, S., and Thépaut, J.-N.: The ERA5
770 global reanalysis, *Q. J. Roy. Meteor. Soc.*, 146, 1999–2049, <https://doi.org/10.1002/qj.3803>, 2020.

771

772 Hjort, J., Karjalainen, O., Aalto, J., *et al.*: Degrading permafrost puts Arctic infrastructure at risk by
773 mid-century, *Nat. Commun.*, 9, 5147, <https://doi.org/10.1038/s41467-018-07557-4>, 2018.

774

775 Hjort, J., Streletskiy, D., Doré, G., *et al.*: Impacts of permafrost degradation on infrastructure, *Nat.*
776 *Rev. Earth Environ.*, 3, 24–38, <https://doi.org/10.1038/s43017-021-00247-8>, 2022.

777

778 Hock, R.: Temperature index melt modelling in mountain areas, *Journal of Hydrology*, 282(1–4),
779 104–115, [https://doi.org/10.1016/S0022-1694\(03\)00257-9](https://doi.org/10.1016/S0022-1694(03)00257-9), 2003.

780

781 Holloway, J. E., Lewkowicz, A. G., Douglas, T. A., *et al.*: Impact of wildfire on permafrost
782 landscapes: A review of recent advances and future prospects, *Permafrost and Periglac. Process.*,
783 31, 371–382, <https://doi.org/10.1002/ppp.2048>, 2020.

784

785 Hu, G., Zhao, L., Wu, T., Wu, X., Park, H., Li, R., *et al.*: Continued warming of the permafrost
786 regions over the Northern Hemisphere under future climate change, *Earth's Future*, 10,
787 e2022EF002835, <https://doi.org/10.1029/2022EF002835>, 2022.

788

789 Hu, G., Zhao, L., Li, R., Park, H., Wu, X., Su, Y., Guggenberger, G., Wu, T., Zou, D., Zhu, X.,
790 Zhang, W., Wu, Y., and Hao, J.: Water and heat coupling processes and its simulation in frozen

791 soils: Current status and future research directions, *CATENA*, 222, 106844, ISSN 0341-8162,
792 <https://doi.org/10.1016/j.catena.2022.106844>, 2023
793

794 Iturbide, M., Fernández, J., Gutiérrez, J. M., Bedia, J., Cimadevilla, E., Díez-Sierra, J., Manzanas,
795 R., Casanueva, A., Baño-Medina, J., Milovac, J., Herrera, S., Cofiño, A. S., San Martín, D., García-
796 Díez, M., Hauser, M., Huard, D., and Yelekci, Ö.: Repository supporting the implementation of
797 FAIR principles in the IPCC-WG1 Atlas, Zenodo, <https://doi.org/10.5281/zenodo.3691645>,
798 <https://github.com/IPCC-WG1/Atlas>, 2022.
799

800 Jan, A., and Painter, S. L.: Permafrost thermal conditions are sensitive to shifts in snow timing,
801 *Environ. Res. Lett.*, 15, 084026, 2020.
802

803 Jan, A.: Modeling the role of lateral surface flow in low-relief polygonal tundra, *Permafrost and*
804 *Periglac. Process.*, 33(3), 214–225, <https://doi.org/10.1002/ppp.2145>, 2022.
805

806 Ji, H., Nan, Z., Hu, J., Zhao, Y., and Zhang, Y.: On the spin-up strategy for spatial modeling of
807 permafrost dynamics: A case study on the Qinghai-Tibet Plateau, *Journal of Advances in Modeling*
808 *Earth Systems*, 14, e2021MS002750, <https://doi.org/10.1029/2021MS002750>, 2022.
809

810 Jin, H., Huang, Y., Bense, V. F., Ma, Q., Marchenko, S. S., Shepelev, V. V., Hu, Y., Liang, S.,
811 Spektor, V. V., Jin, X., *et al.*: Permafrost degradation and its hydrogeological impacts, *Water*, 14,
812 372, <https://doi.org/10.3390/w14030372>, 2022.
813

814 Karjalainen, O., Aalto, J., Luoto, M., *et al.*: Circumpolar permafrost maps and geohazard indices for
815 near-future infrastructure risk assessments, *Sci. Data*, 6, 190037,
816 <https://doi.org/10.1038/sdata.2019.37>, 2019.
817

818 Karlsson, J., Serikova, S., Vorobyev, S. N., *et al.*: Carbon emission from Western Siberian inland
819 waters. *Nat. Commun.*, 12, 825, <https://doi.org/10.1038/s41467-021-21054-1>, 2021.
820

821 Kim, J.-S., *et al.*: Extensive fires in southeastern Siberian permafrost linked to preceding Arctic
822 Oscillation, *Sci. Adv.*, 6, eaax3308, <https://doi.org/10.1126/sciadv.aax3308>, 2020.

823

824 Kirdyanov, A.V., Saurer, M., Siegwolf, R., Knorre, A. A., Prokushkin, A. S., Churakova
825 (Sidorova), O. V., Fonti M. V., and Büntgen, U.: Long-term ecological consequences of forest fires
826 in the continuous permafrost zone of Siberia, *Environ. Res. Lett.*, 15, 034061, 2020.

827

828 Kirdyanov, A.V., Saurer, M., Arzac, A., Knorre, A. A., Prokushkin, A. S., Churakova (Sidorova),
829 O. V., Arosio, T., Bebhuk, T., Siegwolf, R., and Büntgen, U.: Thawing permafrost can mitigate
830 warming-induced drought stress in boreal forest trees, *Science of the Total Environment*, 912,
831 168858, ISSN 0048-9697, <https://doi.org/10.1016/j.scitotenv.2023.168858>, 2024.

832

833 Khani, H. M., Kinnard, C., Gascoin, S., and Lévesque, E.: Fine-scale environment control on
834 ground surface temperature and thaw depth in a High Arctic tundra landscape, *Permafrost and*
835 *Periglac. Process.*, 34(4), 467–480, <https://doi.org/10.1002/ppp.2203>, 2023.

836

837 Kurylyk, B. L., and Watanabe, K.: The mathematical representation of freezing and thawing
838 processes in variably-saturated, non-deformable soils, *Advances in Water Resources*, 60, 160–177,
839 ISSN 0309-1708, <https://doi.org/10.1016/j.advwatres.2013.07.016>, 2013.

840

841 Kurylyk, B. L.: Engineering challenges of warming, *Nat. Clim. Chang.*, 9, 807–808,
842 <https://doi.org/10.1038/s41558-019-0612-8>, 2019.

843

844 Lamontagne-Hallé, P., McKenzie, J. M., Kurylyk, B. L., and Zipper, S.C.: Changing groundwater
845 discharge dynamics in permafrost regions, *Environ. Res. Lett.*, 13, 084017, 2018.

846

847 Li, X.-Y., Jin, H.-J., Wang, H.-W., Marchenko, S. S., Shan, W., Luo, D.-L., He, R.-X., Spektor, V.,
848 Huang, Y.-D., Li, X.-Y., and Jia, N.: Influences of forest fires on the permafrost environment: A
849 review, *Advances in Climate Change Research*, 12(1), 48–65, ISSN 1674-9278,
850 <https://doi.org/10.1016/j.accre.2021.01.001>, 2021.

851

852 Li, G., Zhang, M., Pei, W., Melnikov, A., Khristoforov, I., Li, R., and Yu, F.: Changes in
853 permafrost extent and active layer thickness in the Northern Hemisphere from 1969 to 2018,

854 Science of the Total Environment, 804, 150182, ISSN 0048-9697,
855 <https://doi.org/10.1016/j.scitotenv.2021.150182>, 2022a.
856

857 Li, C., Wei, Y., Liu, Y., Li, L., Peng, L., Chen, J., *et al.*: Active layer thickness in the Northern
858 Hemisphere: Changes from 2000 to 2018 and future simulations, *Journal of Geophysical Research:*
859 *Atmospheres*, 127, e2022JD036785, <https://doi.org/10.1029/2022JD036785>, 2022b.
860

861 Loranty, M. M., Abbott, B. W., Blok, D., Douglas, T. A., Epstein, H. E., Forbes, B. C., Jones, B.
862 M., Kholodov, A. L., Kropp, H., Malhotra, A., Mamet, S. D., Myers-Smith, I. H., Natali, S. M.,
863 O'Donnell, J. A., Phoenix, G. K., Rocha, A. V., Sonnentag, O., Tape, K. D., and Walker, D. A.:
864 Reviews and syntheses: Changing ecosystem influences on soil thermal regimes in northern high-
865 latitude permafrost regions, *Biogeosciences*, 15, 5287–5313, [https://doi.org/10.5194/bg-15-5287-](https://doi.org/10.5194/bg-15-5287-2018)
866 2018, 2018.
867

868 Makarieva, O., Nesterova, N., Post, D. A., Sherstyukov, A., and Lebedeva, L.: Warming
869 temperatures are impacting the hydrometeorological regime of Russian rivers in the zone of
870 continuous permafrost, *The Cryosphere*, 13, 1635–1659, <https://doi.org/10.5194/tc-13-1635-2019>,
871 2019.
872

873 Mashukov, D. A., Benkova, A. V., Benkova, V. E., *et al.*: Radial growth and anatomic structure of
874 the trunk wood of healthy and stag-headed larch trees on permafrost, *Contemp. Probl. Ecol.*, 14,
875 767–774, <https://doi.org/10.1134/S1995425521070143>, 2021.
876

877 Miner, K. R., Turetsky, M. R., Malina, E., *et al.*: Permafrost carbon emissions in a changing Arctic,
878 *Nat. Rev. Earth Environ.*, 3, 55–67, <https://doi.org/10.1038/s43017-021-00230-3>, 2022.
879

880 Nitzbon, J., Krinner, G., Schneider von Deimling, T., Werner, M., and Langer, M.: First
881 quantification of the permafrost heat sink in the Earth's climate system, *Geophysical Research*
882 *Letters*, 50, e2022GL102053, <https://doi.org/10.1029/2022GL102053>, 2023.
883

884 Nitze, I., Grosse, G., Jones, B. M., *et al.*: Remote sensing quantifies widespread abundance of
885 permafrost region disturbances across the Arctic and Subarctic, *Nat. Commun.*, 9, 5423,
886 <https://doi.org/10.1038/s41467-018-07663-3>, 2018.

887

888 Obu, J., Westermann, S., Bartsch, A., Berdnikov, N., Christiansen, H. H., Dashtseren, A., Delaloye,
889 R., Elberling, B., Etzelmüller, B., Kholodov, A., Khomutov, A., Kääh, A., Leibman, M. O.,
890 Lewkowicz, A. G., Panda, S. K., Romanovsky, V., Way, R. G., Westergaard-Nielsen, A., Wu, T.,
891 Yamkhin, J., and Zou, D., Northern Hemisphere permafrost map based on TTOP modelling for
892 2000–2016 at 1 km² scale, *Earth-Science Reviews*, 193, 299–316, ISSN 0012-8252,
893 <https://doi.org/10.1016/j.earscirev.2019.04.023>, 2019.

894

895 Oehri, J., Schaepman-Strub, G., Kim, J. S., *et al.*: Vegetation type is an important predictor of the
896 arctic summer land surface energy budget, *Nat. Commun.*, 13, 6379,
897 <https://doi.org/10.1038/s41467-022-34049-3>, 2022.

898

899 O’Neill, B. C., Tebaldi, C., van Vuuren, D. P., Eyring, V., Friedlingstein, P., Hurtt, G., Knutti, R.,
900 Kriegler, E., Lamarque, J.-F., Lowe, J., Meehl, G. A., Moss, R., Riahi, K., and Sanderson, B. M.:
901 The Scenario Model Intercomparison Project (ScenarioMIP) for CMIP6, *Geosci. Model Dev.*, 9,
902 3461–3482, <https://doi.org/10.5194/gmd-9-3461-2016>, 2016.

903

904 Orgogozo, L., Prokushkin, A. S., Pokrovsky, O. S., Grenier, C., Quintard, M., Viers, J., and Audry,
905 S.: Water and energy transfer modeling in a permafrost-dominated, forested catchment of Central
906 Siberia: The key role of rooting depth, *Permafrost and Periglacial Processes*, 30, 75–89,
907 <https://doi.org/10.1002/ppp.1995>, 2019.

908

909 Orgogozo, L., Xavier, T., Oulbani, H., and Grenier, C.: Permafrost modelling with OpenFOAM®:
910 New advancements of the permaFoam solver, *Computer Physics Communications*, 282,
911 <https://doi.org/10.1016/j.cpc.2022.108541>, 2023.

912

913 Park, H., Tanoue, M., Sugimoto, A., Ichiyonagi, K., Iwahana, G., and Hiyama, T.: Quantitative
914 separation of precipitation and permafrost waters used for evapotranspiration in a boreal forest: A

915 numerical study using tracer model, *Journal of Geophysical Research: Biogeosciences*, 126,
916 e2021JG006645, <https://doi.org/10.1029/2021JG006645>, 2021.

917

918 Park, S. W., Kim, J. S., and Kug, J. S.: The intensification of Arctic warming as a result of CO₂
919 physiological forcing, *Nat. Commun.*, 11, 2098, <https://doi.org/10.1038/s41467-020-15924-3>, 2020.

920

921 Park, S. W., and Kug, J. S.: A decline in atmospheric CO₂ levels under negative emissions may
922 enhance carbon retention in the terrestrial biosphere, *Commun. Earth Environ.*, 3, 289,
923 <https://doi.org/10.1038/s43247-022-00621-4>, 2022.

924

925 Pokrovsky, O. S., Schott, J. S., Kudryavtzev, D. I., and Dupré, B.: Basalt weathering in Central
926 Siberia under permafrost conditions, *Geochimica et Cosmochimica Acta*, 69(24), 5659–5680, 2005.

927

928 Porter, C., Howat, I., Noh, M.-J., Husby, E., Khuvis, S., Danish, E., Tomko, K., Gardiner, J.,
929 Negrete, A., Yadav, B., Klassen, J., Kelleher, C., Cloutier, M., Bakker, J., Enos, J., Arnold, G.,
930 Bauer, G., and Morin, P., ArcticDEM - Mosaics, Version 4.1, Harvard Dataverse, V1,
931 <https://doi.org/10.7910/DVN/3VDC4W>, 2023.

932

933 Prokushkin, A., Kajimoto, T., Prokushkin, S., McDowell, W., Abaimov, A. P., and Matsuura, Y.:
934 Climatic factors influencing fluxes of dissolved organic carbon from the forest floor in a
935 continuous-permafrost Siberian watershed, *Canadian Journal of Forest Research-Journal Canadien*
936 *de la Recherche Forestiere*, 35, 2130–2140, <https://doi.org/10.1139/x05-150>, 2004.

937

938 Prokushkin, A. S., Gleixner, G., McDowell, W. H., Ruehlow, S., and Schulze, E.-D.: Source- and
939 substrate-specific export of dissolved organic matter from permafrost-dominated forested watershed
940 in central Siberia, *Global Biogeochem. Cycles*, 21, GB4003,
941 <https://doi.org/10.1029/2007GB002938>, 2007.

942

943 Ramage, J., Jungsberg, L., Wang, S., *et al.*: Population living on permafrost in the Arctic, *Popul.*
944 *Environ.*, 43, 22–38, <https://doi.org/10.1007/s11111-020-00370-6>, 2021.

945

946 Revich, B. A., Eliseev, D. O., and Shaposhnikov, D. A.: Risks for public health and social
947 infrastructure in Russian Arctic under climate change and permafrost degradation, *Atmosphere*, 13,
948 532, <https://doi.org/10.3390/atmos13040532>, 2022.

949

950 Rew, L. J., McDougall, K. L., Alexander, J. M., Daehler, C. C., Essl, F., Haider, S., Kueffer, C.,
951 Lenoir, J., Milbau, A., Nuñez, M. A., Pauchard, A., and Rabitsch, W.: Moving up and over:
952 Redistribution of plants in alpine, Arctic, and Antarctic ecosystems under global change, *Arctic,
953 Antarctic, and Alpine Research*, 52(1), 651–665, <https://doi.org/10.1080/15230430.2020.1845919>,
954 2020.

955

956 Schneider von Deimling, T., Lee, H., Ingeman-Nielsen, T., Westermann, S., Romanovsky, V.,
957 Lamoureux, S., Walker, D. A., Chadburn, S., Trochim, E., Cai, L., Nitzbon, J., Jacobi, S., and
958 Langer, M.: Consequences of permafrost degradation for Arctic infrastructure – bridging the model
959 gap between regional and engineering scales, *The Cryosphere*, 15, 2451–2471,
960 <https://doi.org/10.5194/tc-15-2451-2021>, 2021.

961

962 Schuur, E.A.G., *et al.*: Permafrost and climate change: Carbon cycle feedbacks from the warming
963 Arctic, *Annual Review of Environment and Resources*, 47(1), 343–371, 2022.

964

965 Shiklomanov, N. I., Streletskiy, D. A., Swales, T. B., and Kokorev, V. A.: Climate change and
966 stability of urban infrastructure in Russian permafrost regions: Prognostic assessment based on
967 GCM climate projections, *Geographical Review*, 107(1), 125–142,
968 <https://doi.org/10.1111/gere.12214>, 2017.

969

970 Sjöberg, Y., Coon, E., Sannel, A. B. K., Pannetier, R., Harp, D., Frampton, A., Painter, S. L., and
971 Lyon, S. W.: Thermal effects of groundwater flow through subarctic fens: A case study based on
972 field observations and numerical modeling, *Water Resour. Res.*, 52, 1591–1606,
973 <https://doi.org/10.1002/2015WR017571>, 2016.

974

975 Sonke, J. E., Teisserenc, R., Heimbürger-Boavida, L.-E., Petrova, M. V., Maruszczak, N., Le Dantec,
976 T., Chupakov, A. V., Li, C., Thackray, C. P., Sunderland, E. M., Tananaev, N., and Pokrovsky, O.
977 S.: Eurasian river spring flood observations support net Arctic Ocean mercury export to the
978 atmosphere and Atlantic Ocean, *PNAS*, 115, 50, E11586–E11594,
979 www.pnas.org/cgi/doi/10.1073/pnas.1811957115, 2018.

980

981 Speetjens, N. J., Hugelius, G., Gumbricht, T., Lantuit, H., Berghuijs, W. R., Pika, P. A., Poste, A.,
982 and Vonk, J. E.: The pan-Arctic catchment database (ARCADE), *Earth Syst. Sci. Data*, 15, 541–
983 554, <https://doi.org/10.5194/essd-15-541-2023>, 2023.

984

985 Streletskiy, D. A., Suter, L. J., Shiklomanov, N. I., Porfiriev, B. N., and Eliseev, D. O.: Assessment
986 of climate change impacts on buildings, structures and infrastructure in the Russian regions on
987 permafrost, *Environ. Res. Lett.*, 14, 025003, 2019.

988

989 Streletskiy, D. A., Clemens, S., Lanckman, J.-P., and Shiklomanov, N. I.: The costs of Arctic
990 infrastructure damages due to permafrost degradation, *Environ. Res. Lett.*, 18, 015006,
991 <https://doi.org/10.1088/1748-9326/acab18>, 2023.

992

993 Stuenzi, S. M., Boike, J., Gädeke, A., Herzsuh, U., Kruse, S., Pestryakova, L. A., Westermann,
994 S., and Langer, M.: Sensitivity of ecosystem-protected permafrost under changing boreal forest
995 structures, *Environ. Res. Lett.*, 16, 084045, <https://doi.org/10.1088/1748-9326/ac153d>, 2021.

996

997 van Vuuren, D. P., Edmonds, J., Thomson, A., Riahi, K., Kainuma, M., Matsui, T., Hurtt, G. C.,
998 Lamarque, J.-F., Meinshausen, M., Smith, S., Granier, C., Rose, S. K., and Hibbard, K. A.: The
999 representative concentration pathways: An overview, *Climatic Change*, 109, 5–31,
1000 <https://doi.org/10.1007/s10584-011-0148-z>, 2011.

1001

1002 Viers, J., Prokushkin, A. S., Pokrovsky, O. S., *et al.*: Seasonal and spatial variability of elemental
1003 concentrations in boreal forest larch foliage of Central Siberia on continuous permafrost,
1004 *Biogeochemistry*, 113(1-3), 435–449, <https://doi.org/10.1007/s10533-012-9770-8>, 2013.

1005

1006 Vitasse, Y., Porté, A. J., Kremer, A., *et al.*: Responses of canopy duration to temperature changes in
1007 four temperate tree species: Relative contributions of spring and autumn leaf phenology, *Oecologia*,
1008 161, 187–198, <https://doi.org/10.1007/s00442-009-1363-4>, 2009.

1009

1010 Vitasse, Y., François, C., Delpierre, N., Dufrêne, E., Kremer, A., Chuine, I., and Delzon S.:
1011 Assessing the effects of climate change on the phenology of European temperate trees, *Agricultural
1012 and Forest Meteorology*, 151(7), 969–980, ISSN 0168-1923,
1013 <https://doi.org/10.1016/j.agrformet.2011.03.003>, 2011.

1014

1015 Vonk, J. E., Speetjens, N. J., and Poste, A. E.: Small watersheds may play a disproportionate role in
1016 arctic land-ocean fluxes, *Nat. Commun.*, 14, 3442, <https://doi.org/10.1038/s41467-023-39209-7>,
1017 2023.
1018

1019 Walvoord, M. A., and Kurylyk, B. L.: Hydrologic impacts of thawing permafrost—A review,
1020 *Vadose Zone Journal*, 15, 1–20, <https://doi.org/10.2136/vzj2016.01.0010>, 2016.
1021

1022 Walvoord, M. A., and Striegl, R. G.: Complex vulnerabilities of the water and aquatic carbon cycles
1023 to permafrost thaw, *Front. Clim.*, 3, 730402, <https://doi.org/10.3389/fclim.2021.730402>, 2021.
1024

1025 Wang, J., and Liu, D.: Vegetation green-up date is more sensitive to permafrost degradation than
1026 climate change in spring across the northern permafrost region, *Global Change Biology*, 28, 1569–
1027 1582, <https://doi.org/10.1111/gcb.16011>, 2022.
1028

1029 Weller, H. G., Tabor, G., Jasak, H., and Fureby, C.: A tensorial approach to computational
1030 continuum mechanics using object orientated techniques, *Computers in Physics*, 12, 620–631,
1031 <https://doi.org/10.1063/1.168744>, 1998.
1032

1033 Westermann, S., Barboux, C., Bartsch, A., Delaloye, R., Grosse, G., Heim, B., Hugelius, G.,
1034 Irrgang, A., Käab, A. M., Matthes, H., Nitze, I., Pellet, C., Seifert, F. M., Strozzi, T., Wegmüller,
1035 U., Wieczorek, M., and Wiesmann, A.: ESA Permafrost Climate Change Initiative
1036 (Permafrost_cci): Permafrost active layer thickness for the Northern Hemisphere, v4.0, NERC EDS
1037 Centre for Environmental Data Analysis, 24 April 2024,
1038 <https://doi.org/10.5285/d34330ce3f604e368c06d76de1987ce5>, 2024.
1039

1040 Wright, S. N., Thompson, L. M., Olefeldt, D., Connon, R. F., Carpino, O. A., Beel, C. R., and
1041 Quinton, W. L.: Thaw-induced impacts on land and water in discontinuous permafrost: A review of
1042 the Taiga Plains and Taiga Shield, northwestern Canada, *Earth-Science Reviews*, 232, 104104,
1043 ISSN 0012-8252, <https://doi.org/10.1016/j.earscirev.2022.104104>, 2022.
1044

1045 Zellweger, F., Coomes, D., Lenoir, J., *et al.*: Seasonal drivers of understorey temperature buffering
1046 in temperate deciduous forests across Europe, *Global Ecol. Biogeogr.*, 28, 1774–1786,
1047 <https://doi.org/10.1111/geb.12991>, 2019.

1048

1049 Zellweger, F., *et al.*: Forest microclimate dynamics drive plant responses to warming, *Science*, 368,
1050 772–775, <https://doi.org/10.1126/science.aba6880>, 2020.